

REPORT DOCUMENTATION PAGE				Form Approved OMB No. 0704-0188	
<p>The public reporting burden for this collection of information is estimated to average 1 hour per response, including the time for reviewing instructions, searching existing data sources, gathering and maintaining the data needed, and completing and reviewing the collection of information. Send comments regarding this burden estimate or any other aspect of this collection of information, including suggestions for reducing the burden, to the Department of Defense, Executive Service Directorate (0704-0188). Respondents should be aware that notwithstanding any other provision of law, no person shall be subject to any penalty for failing to comply with a collection of information if it does not display a currently valid OMB control number.</p> <p>PLEASE DO NOT RETURN YOUR FORM TO THE ABOVE ORGANIZATION.</p>					
1. REPORT DATE (DD-MM-YYYY) 03/01/2010		2. REPORT TYPE Final Technical		3. DATES COVERED (From - To) 01/01/2007 - 12/31/2009	
4. TITLE AND SUBTITLE NUMERICAL SIMULATION OF HYPERSONIC BOUNDARY LAYER RECEPTIVITY, TRANSIENT GROWTH AND TRANSITION WITH SURFACE ROUGHNESS				5a. CONTRACT NUMBER	
				5b. GRANT NUMBER FA9550-07-1-0414	
				5c. PROGRAM ELEMENT NUMBER	
				5d. PROJECT NUMBER	
6. AUTHOR(S) Xiaolin Zhong				5e. TASK NUMBER	
				5f. WORK UNIT NUMBER	
7. PERFORMING ORGANIZATION NAME(S) AND ADDRESS(ES) Mechanical and Aerospace Engineering Department University of California, Los Angeles, CA 90095				8. PERFORMING ORGANIZATION REPORT NUMBER	
9. SPONSORING/MONITORING AGENCY NAME(S) AND ADDRESS(ES) AIRFORCE OFFICE OF SCIENTIFIC RESEARCH, AFOSR/NA 875 North Randolph Street Suite 325, Room 3112 Arlington, Virginia 22203				10. SPONSOR/MONITOR'S ACRONYM(S)	
				11. SPONSOR/MONITOR'S REPORT NUMBER(S)	
12. DISTRIBUTION/AVAILABILITY STATEMENT APPROVED FOR PUBLIC RELEASE DISTRIBUTION IS UNLIMITED					
13. SUPPLEMENTARY NOTES					
14. ABSTRACT <p>The objective of this research is to conduct DNS studies of hypersonic boundary layer receptivity, transient growth and transition with surface roughness. The main approach is to use DNS as a research tool to study the boundary layer receptivity and transient-growth mechanisms in hypersonic flows, including the development of numerical algorithms and parallel computer codes of higher order numerical methods for the simulation of hypersonic flows with surface roughness of finite heights. During the three-year period, we have conducted DNS studies on the hypersonic boundary layer flows over flat plates and blunt cones. A new high-order cut-cell method has been developed for the numerical simulation of hypersonic boundary layer transition with finite height surface roughness. The method has been applied to the numerical simulations of two-dimensional hypersonic flows over a flat plate. Furthermore, the stabilization effect of the surface porous coating over a flat plate is extensively studied by series of numerical simulations. We also collaborate with Prof. Tumin in the University of Arizona to compare numerical and theoretical results on receptivity of a Mach 5.92 flow over a flat plate to wall blowing-suction, and to analyze the nonparallel flow effect.</p>					
15. SUBJECT TERMS <p>HYPERSONIC BOUNDARY LAYER, RECEPTIVITY, TRANSIENT GROWTH, TRANSITION, DIRECTION NUMERICAL SIMULATION, HIGH-ORDER CUT-CELL METHODS.</p>					
16. SECURITY CLASSIFICATION OF:			17. LIMITATION OF ABSTRACT UL	18. NUMBER OF PAGES	19a. NAME OF RESPONSIBLE PERSON XIAOLIN ZHONG
a. REPORT	b. ABSTRACT	c. THIS PAGE			19b. TELEPHONE NUMBER (Include area code) (310) 825-2905

FINAL TECHNICAL REPORT

**NUMERICAL SIMULATION OF HYPERSONIC BOUNDARY LAYER
RECEPTIVITY, TRANSIENT GROWTH AND TRANSITION WITH
SURFACE ROUGHNESS**

Grant Number: FA9550-07-1-0414

(01/01/2007 to 12/31/2009)

Xiaolin Zhong

Professor

Mechanical and Aerospace Engineering Department

University of California, Los Angeles

Los Angeles, California 90095-1597

phone: (310) 825-2905

e-mail: xiaolin@seas.ucla.edu

Prepared for:

Air Force Office of Scientific Research

AFOSR/NA

4015 Wilson Boulevard, Room 713

Arlington VA 22203-1954

Grant Monitor: Dr. John Schmisseur/NA

Contents

1	SUMMARY.....	2
2	RESEARCH OBJECTIVES	4
3	RESEARCH ACCOMPLISHMENTS.....	5
3.1	DEVELOPMENT OF A NEW HIGH-ORDER CUT-CELL METHOD	6
3.2	STUDIED THE STABILITY OF A MACH 5.92 FLAT-PLATE BOUNDARY LAYER WITH FINITE HEIGHT ROUGHNESS IN DIFFERENT LOCATIONS.....	8
3.3	STUDIED THE STABILIZATION OF A MACH 5.92 FLAT-PLATE BOUNDARY LAYER USING LOCAL SECTIONS OF POROUS COATINGS	10
3.4	COLLABORATED WITH PROF. TUMIN ON RECEPTIVITY OF THE MACH 5.92 FLOW OVER A FLAT PLATE TO WALL BLOWING-SUCTION	13
3.5	STUDIED THE NOSE-BLUNTNES AND ENTROPY-LAYER EFFECTS ON HYPERSONIC BOUNDARY LAYER IN THE CONTEXT OF TRANSIENT GROWTH WITH OR WITHOUT SURFACE ROUGHNESS.....	13
4	SUMMARY OF RESEARCH ACCOMPLISHMENTS	15
5	DEVELOPMENT OF A NEW HIGH-ORDER CUT-CELL METHOD	16
5.1	INTRODUCTION	16
5.2	HIGH-ORDER CUT-CELL METHOD	20
5.3	TEST AND APPLICATIONS.....	33
6	STABILIZATION OF A MACH 5.92 FLAT-PLATE BOUNDARY LAYER WITH FINITE HEIGHT SURFACE ROUGHNESS.....	33
6.1	FLOW CONDITIONS AND ROUGHNESS MODEL	34
6.5	STABILIZATION EFFECT OF LOCATION OF THE FINITE ROUGHNESS	44
7	PERSONNEL	47
8	PUBLICATIONS	48
9	ACKNOWLEDGEMENT / DISCLAIMER.....	50
10	REFERENCES.....	50

1 SUMMARY

Recent research has shown that one possible explanation to bypass transition is the transient growth theory. However, there has not been any direct numerical simulation study on transient growth in hypersonic boundary layers. Furthermore, it is not known how the optimal disturbances computed by the transient growth theory are generated by surface roughness. It is also not clear what the role of freestream disturbances are in the transient growth theory. These are important issues related to the receptivity of transient growth, which need to be resolved. The understanding of such a complex flow phenomena can best be obtained through a coordinated study involving both computational and theoretical analyses. Direct numerical simulation (DNS) is uniquely suited for such studies because the complete receptivity process and transient growth can be simulated with minimum simplification assumptions. Supported by AFOSR under the Grant number FA9550-04-1-0029 from January 2004 to December 2006, our group at UCLA has demonstrated that our unique high-order shock fitting simulation approach is a powerful tool in studying supersonic and hypersonic boundary-layer stability and transition physics. We have conducted extensive DNS studies on the flow mechanisms of hypersonic boundary layer receptivity and stability. Our computer code is fully validated by comparing numerical simulation solutions with available experimental or theoretical results on hypersonic boundary layer receptivity and stability.

The objective of the three-year research is to conduct DNS studies of hypersonic boundary layer receptivity, transient growth and transition with surface roughness. The main approach of the proposed research is to use DNS as a research tool to study the boundary layer receptivity and transient-growth mechanisms in hypersonic flows, including the development of numerical algorithms and parallel computer codes of higher order numerical methods for the simulation of hypersonic flows with surface roughness of finite heights. During the three-year period, we have conducted DNS studies on the hypersonic boundary layer flows over flat plates and blunt cones. A new high-order cut-cell method has been developed for the numerical simulation of hypersonic boundary layer transition with finite height surface roughness. The method has been applied to the numerical simulations of two-dimensional hypersonic flows over a flat plate. Furthermore, the stabilization effect of the surface porous coating over a flat plate is extensively studied by series of numerical simulations. We also collaborate with Prof. Tumin in the University of Arizona to compare numerical and theoretical results on receptivity of a Mach 5.92 flow over a flat plate to wall blowing-suction, and to deeply analyze the nonparallel flow effects. Our numerical studies have been validated to be of high accuracy and led to further understanding of hypersonic boundary layer receptivity mechanism. Such understanding can lead to better tool for the prediction and control of high speed boundary layer transition.

The main research contributions are:

1. We have developed a new high-order cut-cell method for the numerical simulation of hypersonic boundary layer transition with finite height surface roughness. Parallel computer codes of the numerical method have been implemented. The new high-order cut-cell method has been

tested in the computations of several one and two-dimensional hyperbolic and elliptic equation in irregular domains. The results show that up to fourth-order accuracy in both L^2 and L^∞ norm can be obtained for the current cut-cell method for both problems.

2. We subsequently have applied a third-order cut-cell method to the two-dimensional compressible Navier-Stokes equations for simulating roughness induced receptivity for hypersonic flow over a flat plate with a blowing and suction slot placed near the leading edge. The surface roughness height is approximately half of the local boundary thickness. The results show that the roughness location plays an important role in the developments of mode S initially excited by the blowing-suction actuator. Mode S is destabilized only when the roughness element is located close upstream of the synchronization point. On the other hand, when the roughness element is downstream of the synchronization point, mode S is stabilized. This happens even when the roughness is still within the unstable region of mode S. Therefore, the synchronization point and finite roughness location is critical to the receptivity process.
3. We have extensively studied the stabilization of a Mach 5.92 flat-plate boundary layer using local sections of porous coating by series of numerical simulations. The stabilization effect of porous coating on hypersonic boundary layers over flat plates and cones has been successfully demonstrated by theoretical analyses, experiments, and numerical simulations. It has been found that porous coating slightly destabilizes the Mack first mode whereas it significantly stabilizes the Mack second mode. In previous studies, porous coating covers either the entire flat plate or the surface around half the cone circumference. The effect of porous coating locations on boundary layer stabilizations has not been considered. Furthermore, the destabilization effect of porous coating on the Mack first mode has not been studied in detail. In our numerical simulations, we focus on the effect of porous coating locations and the destabilization of the Mack first mode. It is found that the synchronization point of mode S and mode F plays an important role on boundary layer stabilization. Disturbances are destabilized when porous coating is located upstream of the synchronization point whereas they are stabilized when porous coating is downstream of the synchronization point. For felt-metal porous coating, destabilization of the Mack first mode is significant.
4. We collaborate with Prof. Tumin in the University of Arizona to compare numerical and theoretical results on receptivity of the Mach 5.92 flow over a flat plate to wall blowing-suction, and to deeply analyze the nonparallel flow effects. The perturbation flow field is decomposed into normal modes with the help of the multimode decomposition technique based on the spatial biorthogonal eigenfunction system. The decomposition allows filtering out the stable and unstable modes hidden behind perturbations having another physical nature. The results indicate that nonparallel flow effects stabilize the second mode whereas destabilize the first mode.
5. We have also conducted numerical simulation studies of Stetson's Mach 5.5 experiments on the nose bluntness effects. Three nose radii of 0.0156in, 0.5in, and 1.5in are used to study the nose bluntness effects on boundary layer instability and transition. The simulation results show that

the increase of nose bluntness leads to the substantial decrease in local Reynolds numbers along the edge of the boundary layers.

2 RESEARCH OBJECTIVES

The prediction of laminar-turbulent transition in supersonic and hypersonic boundary layers is a critical part of the aerodynamics and heating analyses for the development of hypersonic transportation vehicles and re-entry vehicles. The key for an accurate transition prediction is the understanding of the physical mechanisms that lead to transition. However, many important physical mechanisms leading to hypersonic boundary layer transition are currently still not well understood. Recent research has shown that one possible explanation to bypass transition is the transient growth theory. However, there has not been any direct numerical simulation study on transient growth in hypersonic boundary layers. Furthermore, it is not known how the optimal disturbances computed by the transient growth theory are generated by surface roughness. It is also not clear what the role of freestream disturbances are in the transient growth theory. These are important issues related to the receptivity of transient growth, which need to be resolved. Due to the difficulties in conducting hypervelocity experiments and the complexity of hypersonic flows, fundamental hypersonic studies increasingly rely on the use of DNS as a research tool. In recent years, DNS has become a powerful tool in the studies of the stability and receptivity of supersonic and hypersonic boundary layers.

Supported by AFOSR, we have developed high-order shock-fitting DNS methods [1], which can be directly applied to hypersonic boundary layers over realistic blunt bodies with the effects of nose bluntness, the presence of bow shock waves, and the real-gas effects at high temperatures. In the past several years, we have studied the receptivity and stability of a number of 2-D and 3-D hypersonic flows over flat plates [2-6], and blunt cones [7-10].

The main **objectives** of this research are to conduct extensive direct numerical simulation studies on the early stage of hypersonic boundary layer receptivity, transient growth, and transition for blunt cones and flat plates, and to develop numerical algorithms and parallel computer codes of higher order numerical methods for the simulation of hypersonic flows with surface roughness of finite heights. The effects of surface roughness, nose bluntness, and freestream disturbances are studied by numerical simulations.

The project has been carried out in three years with the following research tasks:

1. **Development of new high-order direct numerical simulation methods and 3-D computer codes to simulate arbitrary surface roughness effects.** A new high-order cut-cell method for the numerical simulation of hypersonic boundary layer transition with finite height surface roughness [3, 4]. Parallel computer codes of the numerical method have been implemented. The new high-order cut-cell method has been tested in the computations of several one and two-dimensional hyperbolic and elliptic equation

in irregular domains. The results show that up to fourth-order accuracy in both L^2 and L^∞ norm can be obtained for the current cut-cell method for both problems. We subsequently have applied a third-order cut-cell method to the two-dimensional compressible Navier-Stokes equations for simulating roughness induced receptivity for hypersonic flow over a flat plate with a blowing and suction slot placed near the leading edge. The surface roughness height is approximately half of the local boundary thickness.

2. **DNS studies of the stabilization of a Mach 5.92 flat-plate boundary layer using local sections of porous coating.** In our numerical simulations [2], we focus on the effect of porous coating locations and the destabilization of the Mack first mode. It is found that the synchronization point of mode S and mode F plays an important role on boundary layer stabilization. Disturbances are destabilized when porous coating is located upstream of the synchronization point whereas they are stabilized when porous coating is downstream of the synchronization point. For felt-metal porous coating, destabilization of the Mack first mode is significant.
3. **Collaborate with Prof. Tumin in the University of Arizona to compare numerical and theoretical results on receptivity of the Mach 5.92 flow over a flat plate to wall blowing-suction, and to deeply analyze the nonparallel flow effects [6].** The perturbation flow field is decomposed into normal modes with the help of the multimode decomposition technique based on the spatial biorthogonal eigenfunction system. The decomposition allows filtering out the stable and unstable modes hidden behind perturbations having another physical nature. The results indicate that nonparallel flow effects stabilize the second mode whereas destabilize the first mode.
4. **DNS studies of nose-bluntness and entropy-layer effects on hypersonic boundary layer in the context of transient growth with or without surface roughness.** We conduct DNS investigations of transition reversal due to the nose bluntness effects for hypersonic boundary layer over blunt cones and blunt flat plates [10, 11]. A large number of test cases of various nose bluntness, Mach numbers, surface roughness, and Reynolds numbers are studied. We study the nose bluntness effects in the context of receptivity, transient growth, and subsequent development of instability waves.

3 RESEARCH ACCOMPLISHMENTS

The research project described in the previous section was carried out in a three period from January 1, 2007 to December 31, 2009. The three-year research project supported by this grant has led to the publications of

1. **Six** papers in the archive journals or book chapters,

2. **Eighteen** conference papers (mainly AIAA papers),

More importantly, the research has produced a large amount of new results, and has led to new understanding of a number of hypersonic boundary layer receptivity mechanisms. The understanding of the receptivity process is the key to improve current hypersonic boundary layer transition prediction methods. In the following sections, the major research accomplishments are summarized, followed by a more details discussions of some of our new results in hypersonic boundary layer receptivity.

3.1 Development of a new high-order cut-cell method

Publications: [1], [7], [18]

During the three-year project, we developed a new high-order cut cell method for computing boundary layer transition with surface roughness. Due to the difficulty in grid generation for numerical simulation of high-speed flow with arbitrary surface roughness elements, it is advantageous to use a fixed-grid cut-cell method to compute such flow. The grid can be a smooth curvilinear body-fitted one along a baseline smooth surface without the roughness. The actual surface with roughness will cut across the grid lines, which create irregular grid points. Most of the previous Cartesian-grid cut-cell (or sharp-interface) methods with different boundary treatments, however, are only first or second order accurate at the interface. The relative low accuracy at the interface may not be sufficient for numerically simulating laminar-turbulent boundary-layer transition involving surface roughness. For a simulation study of hypersonic boundary layer transition shown in Fig. 1, it is necessary to consider the effects of both a bow shock and an arbitrary roughness element on the lower surface. More details can be found in [1]. Numerical methods for such studies need to be high-order accurate both in resolving the complex shock/disturbance interaction and in resolving a wide range of flow time and length scales. In addition, high-order accuracy is required for the local finite difference schemes for local region adjacent to the surface of the roughness element. In this paper, we present a new high-order cut-cell method for numerical simulation of roughness induced transition in viscous hypersonic boundary-layer flows. This method is mainly based on finite difference method, and is different in implementation from all the methods discussed above. To overcome the small cell problem, we adopt Gibou and Fedkiw's shifting-interpolation-stencil strategy, i.e., the "drop point" approach. The new cut-cell method is uniformly high-order for both regular and irregular grid points. The computational accuracy of our third and fourth order accurate cut-cell methods is tested for the computations of Poisson and hyperbolic equation with Dirichlet boundary conditions in irregular domains. We then test a third-order accurate cut-cell method for the two-dimensional Navier-Stokes equations. The new scheme is used to simulate steady and unsteady hypersonic boundary layer flows over a flat plate with an isolated surface roughness element (Fig. 1). The bow shock generated from the leading edge of the flat plate is treated as a computational boundary and discretized based on Zhong's [1] high-order finite-difference shock-fitting method. The unsteady flow over flat plate is excited by a narrow blowing and suction slot composed of 15 different frequencies mounted near the leading edge. Several multi-dimensional cases are tested to demonstrate the order of accuracy

for these numerical methods.

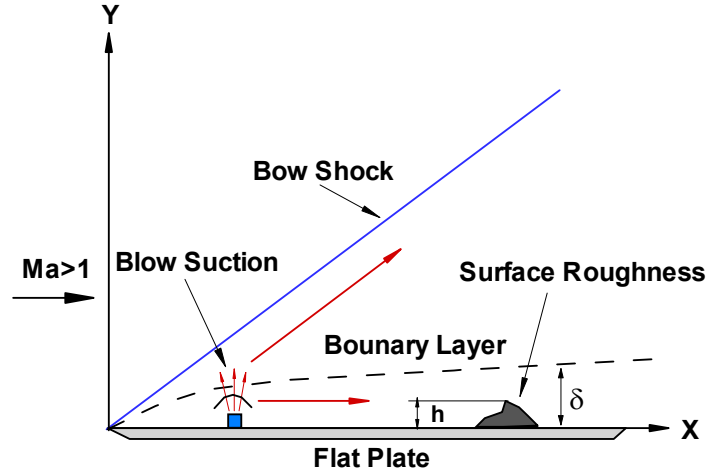


Fig. 1. An example hypersonic flow over flat plate with surface roughness induced boundary layer transition.

Figure 2 shows the numerical solution of an elliptic equation in an irregular domain given by $u_{xx} + u_{yy} = \int_{\Gamma} 2\delta(x - X(s))\delta(y - Y(s))ds$. The interface Γ is a circle defined by $x^2 + y^2 = 1/4$. The computational domain is $(x, y) \in [-1, 1]^2$. A fourth order cut cell method is used to compute the two-dimensional example and the exact solution for the case of 80×80 grids. This figure shows a very good agreement between the exact and numerical solutions. There is no spurious oscillation for the numerical solutions in the region adjacent to the interface.

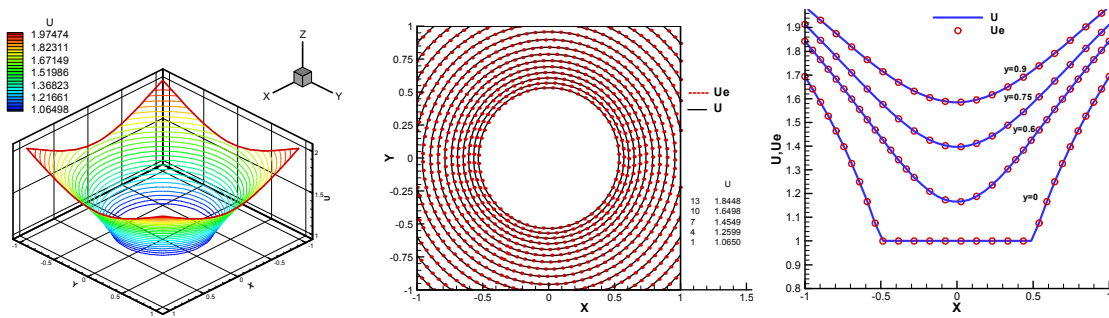


Fig. 2. Comparison of the solution, $u(x, y)$, computed by Version 2 of the fourth-order cut-cell method ($O(h^4)$) for the two-dimensional example and the exact (u_e) (grid: 80×80): 1) and 2) are contours of the solution, 3) is distribution along the x direction.

Table 1 shows the computational errors, in L^∞ and L^2 norms respectively, with four different grid sets. As expected, table 1 shows that the orders in infinity norm are lower than those of the second norm. Overall, the fourth-order cut-cell method with third-order boundary closure schemes produces a fourth-order global accuracy in L^2 norm for the solutions to the two-dimensional problem.

Table 1. Computational errors in L^2 norm of the two versions of the cut-cell methods ($O(h^3)$ and $O(h^4)$) for the two-dimensional test case of LeVeque and Li [12].

<i>Cut Cell Method 1</i>					<i>Cut Cell Method 2</i>			
N	Θ	$\ E_N\ _2$	<i>Ratio</i>	P	Θ	$\ E_N\ _2$	<i>Ratio</i>	P
20	0.5	4.791(-4)			1.0	1.967(-4)		
40	0.5	4.040(-5)	11.9	3.56	1.0	1.437(-5)	13.7	3.77
80	0.5	2.919(-6)	9.54	3.25	1.0	9.049(-7)	15.9	3.99
160	0.5	2.945(-7)	9.91	3.30	1.0	5.773(-8)	15.7	3.97

3.2 Studied the stability of a mach 5.92 flat-plate boundary layer with finite height roughness in different locations

Publications: [7], [14]

The receptivity of a Mach 5.92 boundary-layer flow over a flat plate with finite surface roughness to periodic two-dimensional wall perturbations is investigated by numerical simulations and linear stability theory (LST). The flow conditions are the same as those of Maslov et al.'s leading-edge experiment [13]. The steady base flow is simulated by solving two-dimensional compressible Navier-Stokes equations with a combination of a fifth-order shock-fitting method and a third-order cut cell scheme. Accuracy of the numerical steady base flow is validated by comparing with the theoretical self-similar boundary-layer solution and the published experimental results. The characteristics of boundary-layer wave modes are identified and evaluated by comparing the results of LST and numerical simulations. In receptivity simulations, blowing-suction is used as the periodic two-dimensional wall perturbation, which is introduced to the steady base flow by a forcing slot located on the flat plate. The effects of finite surface roughness on receptivity process are studied by considering four cases of different roughness location. Fig. 3 compare normalized Mach number and dimensionless streamwise velocity distributions across the boundary layer at three different locations of $x = 0.00096$ m, 0.00121 m, and 0.000138 m. The numerical results agree well with the experimental results and the boundary-layer solution near the plate. However, in the region of $\eta > 5$, the numerical results have a better agreement with the experimental results. The difference between the numerical results and the boundary-layer solution is mainly caused by the

existence of the bow shock, because the effect of the bow shock is neglected in the calculation of the compressible boundary-layer equations.

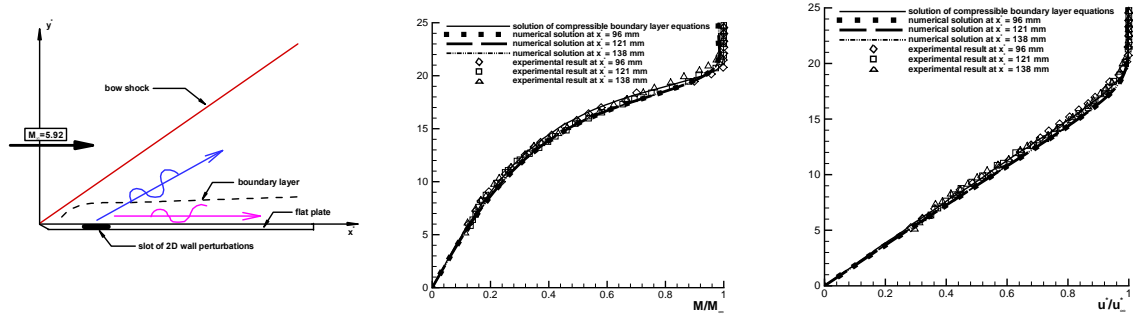


Fig. 3 Numerical simulation of a Mach 5.92 flat-plate boundary layer to two-dimensional wall perturbations and comparisons of normalized Mach number and dimensionless streamwise velocity.

Four cases are simulated by using the high-order cut cell method. Specifically, roughness locations with respect to the synchronization point at $x = 0.331m$ are as follows,

- **Case 1:** Upstream of the synchronization point $x = 0.185m$; The roughness height $h = \frac{1}{2}\delta = 0.00081m$.
- **Case 2:** Upstream of the synchronization point $x = 0.260m$; The roughness height $h = \frac{1}{2}\delta = 0.00111m$.
- **Case 3:** Synchronization point $x = 0.331m$; The roughness height $h = \frac{1}{2}\delta = 0.00141m$
- **Case 4:** Downstream of the synchronization point $x = 0.410m$; The roughness height $h = \frac{1}{2}\delta = 0.00171m$.

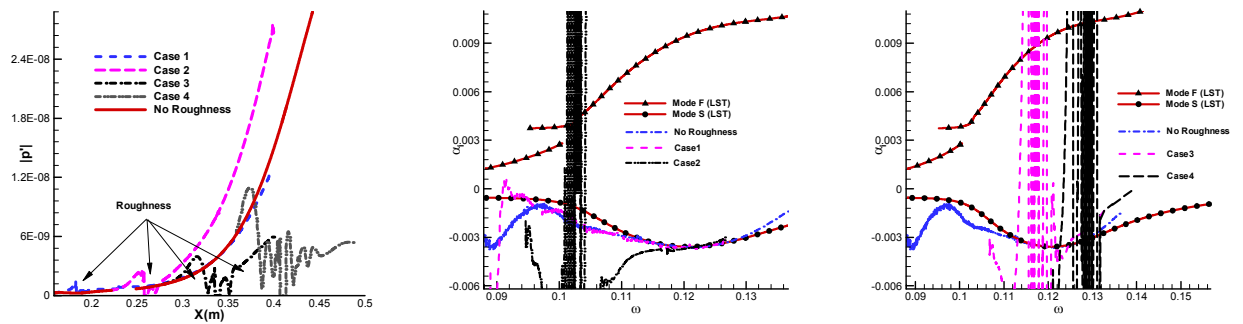


Fig. 4 Numerical simulation of receptivity of the Mach 5.92 flow over a flat plate to two-dimensional wall perturbations with surface roughness: 1) amplitude comparison of pressure, 2) & 3) comparison of numerical and LST growth rates.

Fig. 4 shows the pressure amplitude on the flat plate surface with roughness located in different locations. It shows that for all four cases, the development of two-dimensional wall perturbations eventually result in the same type of instability wave (mode S) in the boundary layer. When the surface roughness located in the far upstream of the synchronization point (Case 1), the instability wave develops in the same way as the case without roughness. But as the roughness moves gradually into the downstream (Case 2), the growth rate of the mode S increases, which reflects that the amplitude of pressure in the flat plate surface is amplified. Mode S is destabilized when the roughness element is placed sufficient close to the synchronization point. In Case 3 and 4, when the roughness located in downstream of synchronization point, the finite surface roughness stabilizes the mode S inside the boundary layer. The amplitude of pressure perturbation is reduced in further downstream.

3.3 Studied the stabilization of a mach 5.92 flat-plate boundary layer using local sections of porous coatings

Publications: [3], [9], [13], [15], [20]

Passive control of boundary layer transition by using porous coating to stabilize hypersonic boundary layers over flat plates and cones has been successfully demonstrated by theoretical analyses, experiments, and numerical simulations [14-18]. Fedorov et al. [14] performed theoretical analyses on the second-mode stability of a hypersonic boundary layer over a flat plate covered by an ultrasonically absorptive coating (UAC). They found that the second mode growth was massively reduced, because the porous layer absorbed the disturbance energy. To demonstrate the stabilization effect of UAC on the second mode, Rasheed et al. [15] experimentally studied the stability of a Mach 5 boundary layer on a sharp 5.06-deg half-angle cone at zero angle of attack. The cone had a smooth surface around half the cone circumference and an UAC porous surface on the other half. Their experiments indicated that the porous surface was highly effective in stabilizing the second mode and delaying transition, when the pore size was significantly smaller than the disturbance wavelength. Fedorov et al. [16] experimentally and theoretically studied the effect of an UAC on hypersonic boundary layer instabilities. Their experiments were performed on a 7-degree half-angle sharp cone in a Mach 6 wind tunnel. Half-surface of the cone was solid whereas the other half-surface was covered by a felt-metal coating. Both theoretical predictions and experimental measurements on two- and three-dimensional disturbances showed that the porous coating strongly stabilized the second mode and marginally destabilized the first mode. Maslov [17] experimentally studied the stabilization of hypersonic boundary layer by micro structural porous coating. In his experiments, both regular porous UAC and random felt-metal porous UAC are used. The results confirmed that porous coating strongly stabilizes the second mode and marginally destabilizes the first mode. Compared with regular structure UAC, felt-metal UAC is much stronger in first mode destabilization, with the peak amplitude of the first mode increasing around 70%. Egorov et al. [18] studied the effect of porous coating on stability and receptivity of a Mach 6 flat-plate boundary layer by two-dimensional numerical simulation using a second-order TVD scheme. They found that a porous coating of regular porosity effectively diminishes the second mode growth rate, while weakly affecting acoustic waves.

In previous studies, porous coating covers either the entire flat plate or the surface around half the cone circumference. The effect of porous coating locations on boundary layer stabilizations has not been considered. Furthermore, the destabilization effect of porous coating on the Mack first mode has not been studied in detail. However, how to locate porous coatings may affect the efficiency of the boundary layer stabilization. The first mode at a given frequency is spatially developed into the second mode at the same frequency when propagating downstream. Therefore, destabilization of the first mode decreases the efficiency of the second mode stabilization. In current research, the stabilization of a Mach 5.92 boundary layer over a flat plate using local sections of porous coating is studied by a combination of direct numerical simulation (DNS) and linear stability theory (LST), focusing on the effect of porous coating locations and the destabilization of the Mack first mode. The stability simulations consist of two steps: 1. periodic disturbances corresponding to mode S or mode F are superimposed on steady base flow at a cross-section of the boundary layer to show spatial development of the wave; 2. local sections of porous coating are used downstream of the superimposed wave to investigate its effect on boundary layer instability. The model of the felt-metal porous coating is the same as that of Fedorov et al. [16]. At step 2, a series of numerical simulations are carried out by putting porous coatings both upstream and downstream of the synchronization point. Numerical simulation results are interpreted by comparing with the theoretical analyses of LST.

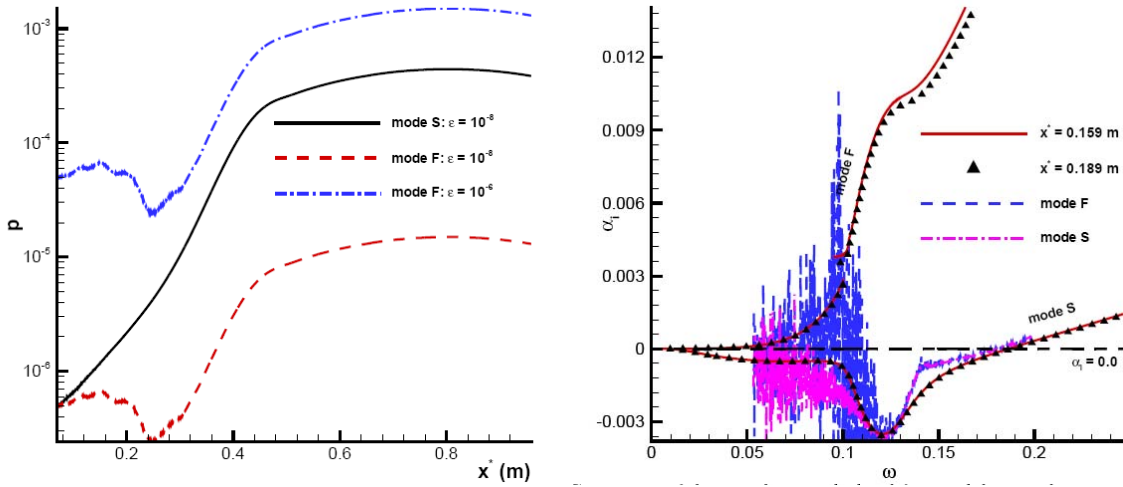


Fig. 5 Spatial developments of superimposed mode S and mode F: pressure amplitude and growth rates

Fig. 6 shows the spatial developments of superimposed mode S and mode F. Periodic disturbances corresponding to mode S or mode F at a frequency of 100 kHz is superimposed on steady base flow at a cross-section of the boundary layer at $x^* = 69.00$ mm ($R = 987.24$). In this figure, the spatial development of superimposed mode F with an amplitude parameter being 10^{-8} is also plotted. It is clearly shown that the spatial developments of mode F with different amplitudes have the same profile. One hundred times difference in superimposed disturbance amplitude leads to 100 times amplitude difference in spatial development, which illustrates the linear properties of disturbances. After mode S is superimposed at $x^* = 69.00$ mm, it grows dramatically with the peak of amplitude being around $x^* = 0.8$ m. The scenario of mode F is quite different from that of mode S. After the

transient process, amplitude of mode F is decreasing because mode F is a stable wave. The lowest amplitude of mode F is observed at around $x^* = 0.24$ m. Then the wave grows quite similar to mode S, also with the peak of amplitude being around $x^* = 0.8$ m.

Fig. 7 also compares the growth rate calculated from stability simulations with that obtained from LST for superimposed mode S and mode F. For mode S, the growth rate of stability simulation has a good agreement with that of LST in the region from $\omega = 0.11$ to $\omega = 0.13$. When ω is larger than 0.13, the growth rate of stability simulation is larger than that of LST, i.e., mode S obtained by stability simulation becomes more stable than that predicted by LST. For mode F, the figure shows that the growth rate of stability simulation initially has a good agreement with that of LST. However, it approaches that of mode S near the synchronization point, which indicates that mode F changes to mode S near the synchronization point. After the change, the growth rate of stability simulation has a good agreement with that of mode S. The discrepancy between the growth rates of mode S calculated from stability simulation and LST, when ω is larger than 0.13, is mainly caused by the nonparallel flow effect.

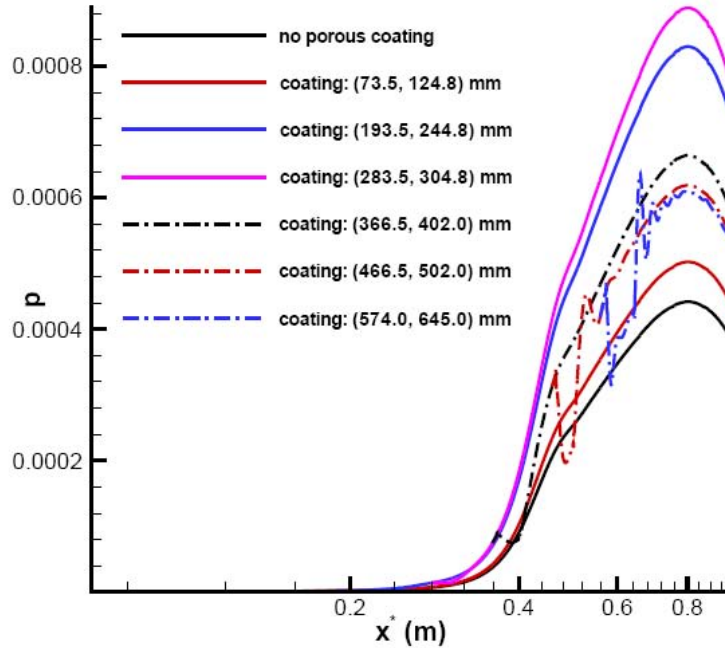


Fig. 8 Amplitude distributions of pressure perturbation along the flat plate.

Fig. 9 shows amplitude distributions of pressure perturbation along the flat plate for the six cases of porous coating, together with the spatial development of mode S. It is noticed that pressure perturbations of all the six cases with porous coating have a similar profile as that of purely mode S without porous coating, both having the peak of amplitude at around $x^* = 0.8$ m. However, porous coating does affect the amplitude of mode S. For cases 1 to 3, porous coatings are upstream of the synchronization point. Amplitude of pressure perturbation increases with the number of porous coating increasing from case 1 to case 3. For cases 4 to 6, porous coatings except the first three are downstream of the synchronization point. Amplitude of pressure perturbation decreases with the number of porous coating increasing from case 4 to case 6. The results show that porous coating destabilizes the Mack first mode whereas it stabilizes the Mack second mode. All the six cases of

stability simulations show larger peak amplitude of mode S, which means destabilization of the Mack first mode is quite significant. In order to control boundary layer transition, it is very important to put porous coating downstream of the synchronization point, where mode S corresponds to the Mack second mode.

3.4 Collaborated with Prof. Tumin on receptivity of the Mach 5.92 flow over a flat plate to wall blowing-suction

Publications: [4], [10], [19]

Direct numerical simulations of receptivity in a boundary layer over a flat plate are carried out with 2D perturbations introduced into the flow by periodic-in-time blowing-suction through a slot [5]. The perturbation flow field was decomposed into normal modes with the help of the multimode decomposition technique based on the spatial biorthogonal eigenfunction system. The decomposition allows filtering out the stable and unstable modes hidden behind perturbations having another physical nature. Method of multiple scales (MMS) is used to investigate the nonparallel flow effects.

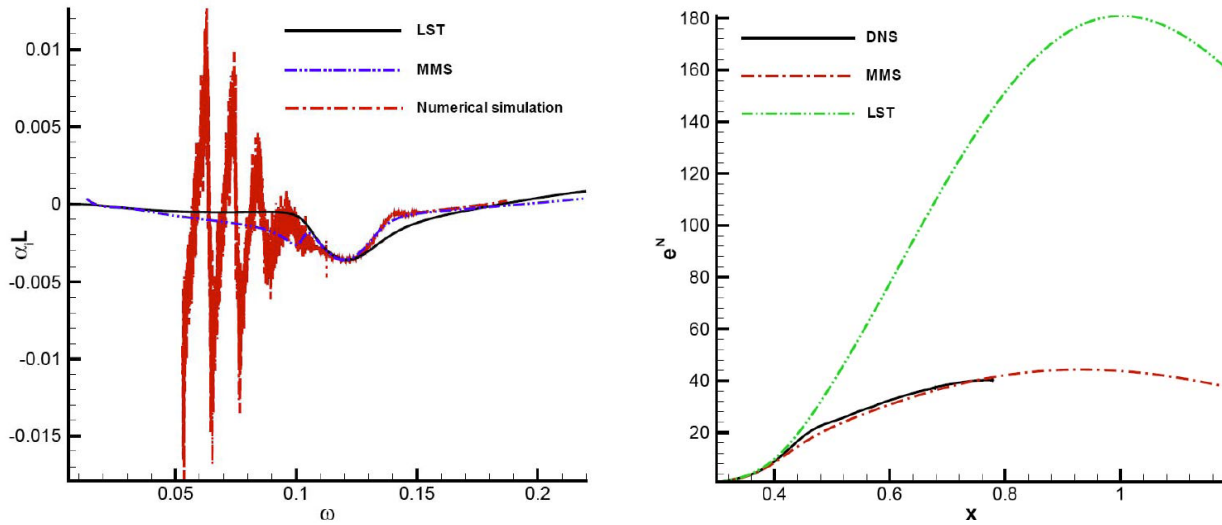


Fig.7 Comparisons of growth rates and pressure perturbation amplitudes.

Fig. 7 compares the growth rates and pressure perturbation amplitude obtained from numerical simulations with those predicted by LST and MMS. Both figures show that the predictions of MMS have a good agreement with the numerical results. Nonparallel flow effects destabilize the first mode whereas stabilize the second mode. Also it is caused by the nonparallel flow effects that, in the numerical simulation results, the growth rate of the second mode is always smaller than that predicted by the linear stability theory.

3.5 Studied the nose-bluntness and entropy-layer effects on hypersonic boundary layer in the context of transient growth with or without surface roughness.

Publications: [16], [24]

For hypersonic boundary layers over blunt cones, the transition reversal phenomenon refers to the experimental observation that the laminar-turbulent transition location moves upstream with increasing nose radius when it is larger than a certain critical value. Currently, there is no satisfactory explanation for transition reversal phenomenon. All previous linear stability theory (LST) and numerical simulation studies on the nose bluntness effects have not found transition reversal. The previous theoretical and computational studies, however, have not been done on the actual experimental flow conditions which had shown transition reversal.

Surface roughness has been shown to have profound effects on boundary layer transition. Recent research has shown that one possible explanation to bypass transition is the transient growth theory. However, there has not been any direct numerical simulation study on transient growth in hypersonic boundary layers. Furthermore, it is not known how the optimal disturbances computed by the transient growth theory are generated by surface roughness. This paper presents some initial results in our on-going numerical simulation study on the receptivity of the hypersonic boundary layers to stationary surface roughness without any freestream forcing waves. The flow conditions are those of Stetson's 1984 wind-tunnel experiments for Mach 7.99 flow over a 7 degree half-angle blunt cone [19]. The simulation results show that the roughness element generates streamwise vortices inside the boundary layer. In the computational domain studied in current project, the induced perturbation mainly decays after the roughness. No strong transient growth appears immediately behind the roughness element.

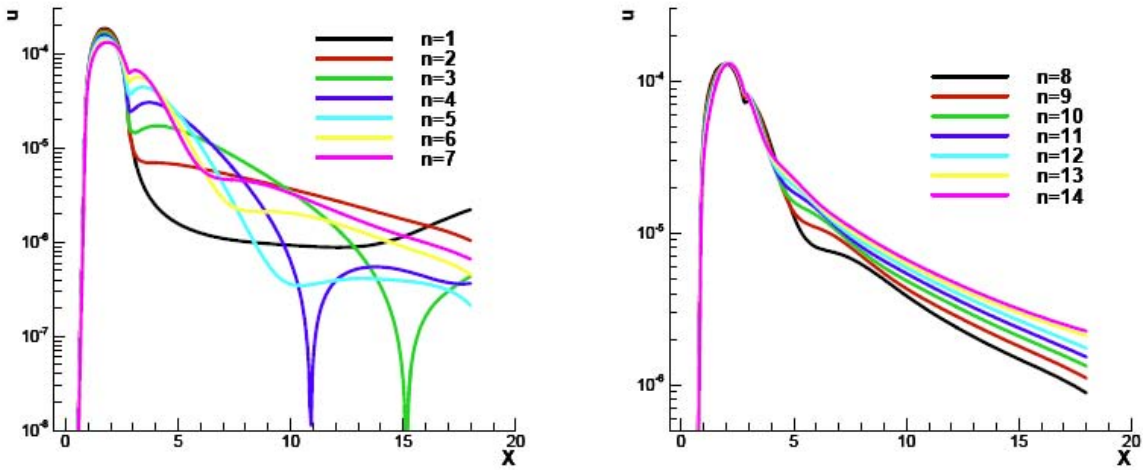


Fig.8 Distributions of u perturbation magnitudes for all 14 modes along a streamwise grid line located near the edge of the boundary layer.

Fig. 8 shows the distribution of u perturbation magnitudes for all 14 modes along a streamwise grid line located near the edge of the boundary layer. The perturbations rise rapidly for flow over the roughness. Downstream of the roughness, the perturbations drop initially for all n . On the other hand, the perturbations for 1 $n =$ start to increase after the initial drop, while the perturbations for

other modes decrease. No obvious strong transient growth can be observed in the current simulation within the limited length of the flow field behind the roughness element.

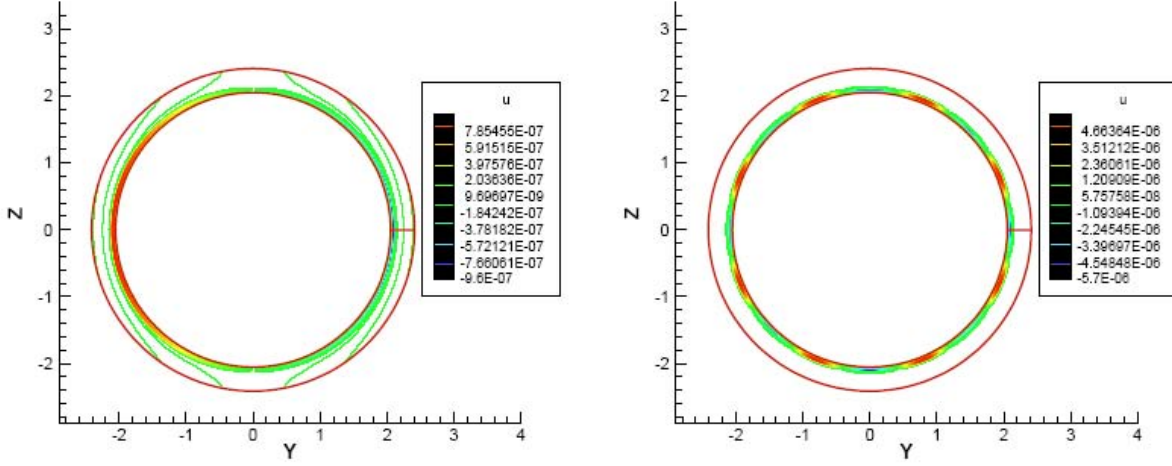


Fig.9 Cross-sectional view of the contours of u perturbations for two of the 14 modes.

Fig. 9 shows the cross-sectional view of the contours of temperature and horizontal velocity perturbations for two of the 14 modes ($n = 1$ and 8). The features for all other modes are similar to those in the figures. For the cases of $n = 1$ and $n = 8$, Fig. 11 shows that the flow decelerates behind the peak of the roughness heights, and accelerates behind the valleys of the roughness element, as a results of the streamwise vortices generated by the surface roughness. The results indicate the generation of the streamwise vortices by the surface roughness.

4 SUMMARY OF RESEARCH ACCOMPLISHMENTS

In the report period, we have mainly focused on the DNS studies of receptivity of supersonic and hypersonic boundary layer flows. A new high-order cut-cell method has been developed for the numerical simulation of hypersonic boundary layer transition with finite height surface roughness. The method has been applied to the numerical simulations of two-dimensional hypersonic flows over a flat plate. Furthermore, the stabilization effect of the surface porous coating over a flat plate is extensively studied by series of numerical simulations. We also collaborate with Prof. Tumin in the University of Arizona to compare numerical and theoretical results on receptivity of a Mach 5.92 flow over a flat plate to wall blowing-suction, and to deeply analyze the nonparallel flow effects. The most significant research accomplishments are

1. We developed a new high-order cut-cell method for computing boundary layer transition with finite surface roughness. Due to the difficulty in grid generation for numerical simulation of high-speed flow with arbitrary surface roughness elements, it is advantageous to use a fixed-grid cut-cell method to compute such flow. Our new method is mainly based on finite difference method, and adopts Gibou and Fedkiw's shifting-interpolation-stencil strategy, i.e., the "drop point" approach, to avoid the "smell cell" problem. The new cut-cell method is uniformly

high-order for all grids in the computational domain. The computational accuracy of our third and fourth order accurate cut-cell methods is tested for the computations of Poisson and hyperbolic equation with Dirichlet boundary conditions in irregular domains. We then test a third-order accurate cut-cell method for the two-dimensional Navier-Stokes equations. The new scheme is used to simulate steady and unsteady hypersonic boundary layer flows over a flat plate with an isolated surface roughness element (Fig. 1).

2. We have studied the stabilization of a Mach 5.92 over a flat plate to two-dimensional wall blowing-suction perturbation with finite roughness located in different locations. The numerical results show that the development of two-dimensional wall perturbations eventually results in the same type of instability wave (mode S) in the boundary layer with roughness. The roughness location plays an important role in the developments of mode S by the blowing-suction actuator. Mode S is destabilized only when the roughness element is located close upstream of the synchronization point. On the other hand, when the roughness element is downstream of the synchronization point, mode S is stabilized. This happens even when the roughness is still within the unstable region of mode S. Therefore, the synchronization point and finite roughness location is critical to the receptivity process. The relationship between the location of the roughness and the synchronization point suggests that, in order to control or delay the laminar-turbulent transition more efficiently, the roughness element should be placed upstream of the synchronization point between mode S and mode F.

5 DEVELOPMENT OF A NEW HIGH-ORDER CUT-CELL METHOD

One major accomplishment of the current research project is the development of a new high-order cut-cell method. Our new method is mainly based on finite difference method, and adopts Gibou and Fedkiw's shifting-interpolation-stencil strategy, i.e., the "drop point" approach, to avoid the "smell cell" problem. The new cut-cell method is uniformly high-order for all grids in the computational domain. The computational accuracy of our third and fourth order accurate cut-cell methods is tested for the computations of Poisson and hyperbolic equation with Dirichlet boundary conditions in irregular domains. We then test a third-order accurate cut-cell method for the two-dimensional Navier-Stokes equations. The new scheme is used to simulate steady and unsteady hypersonic boundary layer flows over a flat plate with an isolated surface roughness element. The new high-order cut-cell method has been tested and published in **Publications: [7], [18]**.

5.1 Introduction

The understanding of physical mechanisms of roughness induced boundary-layer transition is critical to the development of hypersonic vehicles [20]. Transition can have a first-order impact on the lift and drag, stability and control, and heat transfer properties of the vehicles [21]. For example, roughness induced transition is an important consideration in the design of thermal protection systems (TPS) of hypersonic vehicles [22, 23]. Figure 10 shows an example surface roughness on test models for hypersonic boundary layer transition. For a reentry vehicle entering earth's

atmosphere, it initially experiences a heating environment associated with a laminar boundary layer. As the vehicle attitude decreases, the vehicle surface becomes rougher and the boundary layer becomes turbulent. The transition from a laminar boundary layer to a turbulent one leads to the increase of surface heating rates by a factor of five or more. Thus the ability to understand and predict the physics of roughness induced transition plays an essential role in the design of TPS for reentry vehicles. Currently, surface roughness, especially arbitrary roughness induced laminar-turbulent transition in hypersonic boundary layers is still poorly understood due to the limitation in experimental facilities and numerical methods [24].

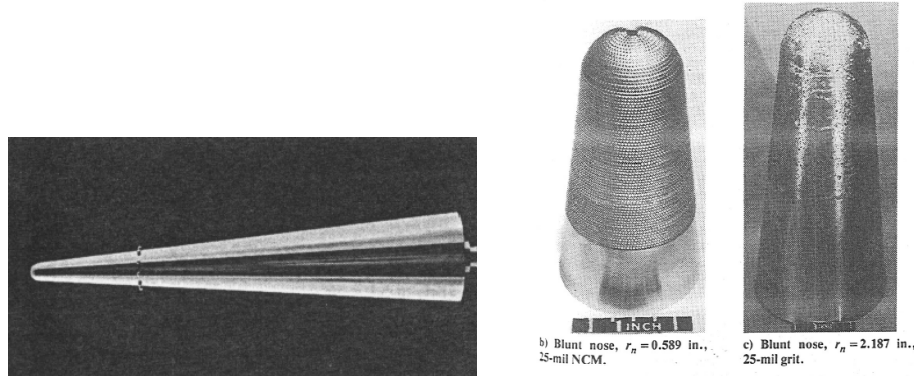


Fig. 10. An example surface roughness on test models for hypersonic boundary layer transition: 1) isolated roughness, 2) distributed roughness [25].

Direct numerical simulation has become an effective research tool for studying hypersonic boundary layer receptivity, stability and transition by numerically solving the time-dependent three-dimensional Navier–Stokes equations for the temporally or spatially evolving instability waves. It is necessary to use high-order numerical methods for the simulation in order to resolve the wide range of length and time scales of the complex wave fields in hypersonic boundary layers. Hence, high-order finite-difference schemes have recently received much attention for the direct numerical simulations of transitional and turbulent flows [26-31]. Zhong [1] presented a fifth-order upwind finite difference shock fitting method for the direct numerical simulation of hypersonic flows with a strong bow shock and with stiff source terms. The use of the shock-fitting method makes it possible to accurately compute the shock-disturbance interactions, and the development of instability waves in the boundary layers. The fifth-order shock-fitting schemes were derived on a uniform grid. For a curvilinear stretched grid, typically used in simulations of viscous flow in a boundary layer, the physical coordinates with a non-uniform grid are first transformed to a uniform grid in the computational coordinates. The high-order schemes are subsequently applied to the transformed equations in a uniform grid. The fifth-order shock-fitting scheme was used for numerical studies of the receptivity of two-dimensional Mach 15 flows over a blunt leading edge [32].

Most of the DNS methods, however, have been developed for smooth surfaces computed by

body-fitted grids. Such methods may not be able to compute flow with surface roughness elements similar to those shown in Fig. 10. The main obstacle is the difficulty in generate smooth body-fitted grids around the surface of arbitrary roughness. One approach for overcoming the difficulty in grid generation is to use a Cartesian grid method, which is easy in grid generation. Cartesian grid methods can also take full advantage of fast computer architectures such as parallel computers and can serve as a very flexible method for simulating flow around complex geometries. On the other hand, a Cartesian grid method, the grid lines are not aligned with the body surface. As a result, special treatment is needed to compute the flow equations in local regions adjacent to the solid surface.

Various Cartesian grid methods have been developed and used to solve problems with arbitrary geometry [33-37]. Peskin developed the immersed boundary method (IBM) [37] for the simulation of blood flow in hearts. The method is based on Cartesian grids where the surface of solid membrane is represented by a discrete delta function. This delta function is added into the Navier-Stokes equations to reflect the immersed boundary between the two phase flows. The resulting equations are discretized by a standard finite difference method in a fixed Cartesian grid system. Since its introduction, the IBM methods have been applied to many different fluid flow problems, including flow interaction with solid surface. For example, Marxen et al. [38] applied the IBM to simulate the effects of a localized two-dimensional roughness element on the disturbance amplification in a hypersonic boundary layer. However, since the immersed boundary method uses the discrete delta function approach, it leads to a smeared interface with a thickness in an order of a mesh width. The immersed boundary method is locally first-order accurate at the interface, which may not be accurate enough for the DNS of hypersonic boundary transition problems.

In contrast to the immersed boundary method with smeared interfaces, “sharp interface” Cartesian grid methods, which maintain second-order accuracy at the interfaces, have been developed [34, 39]. Udaykumar et al. [34, 35] used the finite-volume methodology to solve the incompressible Navier-Stokes equations for flow interacting with moving bodies. The method is based on a fixed Cartesian mesh where the solid boundaries can move across the grid lines. The flow equations are discretized by an overall second-order-accurate finite-volume technique. The interface is represented as a sharp boundary between the fluid and solid phases. A one-sided bilinear interpolation is applied to calculate the accurate flow conditions in the sharp irregular boundary. Johansen, McCorquodale and Colella [39, 40] developed a similar sharp-interface Cartesian grid method for solving two-dimensional Poisson and heat equations on irregular domains. Their method was based on finite-volume formulation, with imbedded irregular grid cells on the boundary. The irregular grid cells were treated by conservative differencing of second-order accurate fluxes on each cell volume. The method is second order accurate for a problem with irregular boundary.

Fedkiw and Gibou [33, 41] developed a ghost fluid method, which is a different implementation of the sharp interface methods, for solving flow equations in arbitrary domain. The basic idea was to extrapolate variables on one side of the boundary into a number of ghost cells located on other side of the solid boundary. The method was uniformly second order. Gibou and Fedkiw [41] improved accuracy of the ghost fluid method to fourth-order accuracy for both the Laplace equation and the

heat equation with Dirichlet boundary conditions on irregular domains. Finite difference discretization was used to solve the equations in an irregular domain. The sharp interface Cartesian grid method has also been termed cut-cell method in handling irregular grid cells along the boundary [42].

For multi-phase flows with moving interfaces, an immersed interface method was developed and has been widely used [43-53]. For an immersed interface method, a Cartesian grid is often used where a sharp interface moves freely across the fixed grid lines. This method can achieve a second or higher order global accuracy by incorporating jump conditions into the finite difference formulas for variables and their derivatives at the interface. This method was first developed by Leveque and Li [12] to solve elliptic equations with discontinuous coefficients and singular sources. The original method was second order in the interior of the domain and locally first order at the interface. Leveque and Li [54] subsequently extended the method to the Stokes flow with elastic boundaries or surface tension. Wiegmann and Bube [46, 47] developed an explicit jump immersed interface method for special cases where the explicit jump conditions of variables and their high-order derivatives are known. This method can only achieve arbitrary high-order accuracy if the corresponding high-order derivatives of jump conditions can be analytically derived. Zhong [53] developed a new high-order immersed interface method which does not require second and higher derivatives of jump conditions. The main idea was to use a wider grid stencil across the interface instead of taking higher derivatives of jump conditions to achieve high-order accuracy for finite difference formulas at the interface.

For sharp-interface Cartesian grid methods, a “small cell problem” [55] of numerical instability would arise when finite-difference or finite-volume methods are applied to relatively small-sized irregular grid cells created by a sharp-interface Cartesian grid method. For a time-dependent problem, the small cell problem will significantly restrict the size of time steps in temporal integration methods. Many methods have been proposed to resolve the small cell problem. Berger and Leveque [55] used a rotating box method. Johansen and Colella [39] used a flux-redistribution procedure. Quirk [56] and Udaykumar [35] employed a cell merging method to avoid small cells in order to maintain numerical stability.

Gibou and Fedkiw [41] presented a stable fourth-order finite difference method for solving the Laplace equation on an irregular domain. They showed that a good rule of thumb for removing small cell restriction is that the interpolation should be shifted to be centered one grid point left or right if the interpolation stencil involves a point considered to be relatively close to the boundary.

Due to the difficulty in grid generation for numerical simulation of high-speed flow with arbitrary surface roughness elements, it is advantageous to use a fixed-grid cut-cell method to compute such flow. The grid can be a smooth curvilinear body-fitted one along a baseline smooth surface without the roughness. The actual surface with roughness will cut across the grid lines, which create irregular grid points. Most of the previous Cartesian-grid cut-cell (or sharp-interface) methods with different boundary treatments, however, are only first or second order accurate at the interface. The relative low accuracy at the interface may not be sufficient for numerically simulating

laminar-turbulent boundary-layer transition involving surface roughness. For a simulation study of hypersonic boundary layer transition shown in Fig. 1, it is necessary to consider the effects of both a bow shock and an arbitrary roughness element on the lower surface. More details can be found in [1]. Numerical methods for such studies need to be high-order accurate both in resolving the complex shock/disturbance interaction and in resolving a wide range of flow time and length scales. In addition, high-order accuracy is required for the local finite difference schemes for local region adjacent to the surface of the roughness element. In this paper, we present a new high-order cut-cell method for numerical simulation of roughness induced transition in viscous hypersonic boundary-layer flows. This method is mainly based on finite difference method, and is different in implementation from all the methods discussed above. To overcome the small cell problem, we adopt Gibou and Fedkiw’s shifting-interpolation-stencil strategy, i.e., the “drop point” approach. The new cut-cell method is uniformly high-order for both regular and irregular grid points. The computational accuracy of our third and fourth order accurate cut-cell methods is tested for the computations of Poisson and hyperbolic equation with Dirichlet boundary conditions in irregular domains. We then test a third-order accurate cut-cell method for the two-dimensional Navier-Stokes equations. The new scheme is used to simulate steady and unsteady hypersonic boundary layer flows over a flat plate with an isolated surface roughness element (Fig. 1). The bow shock generated from the leading edge of the flat plate is treated as a computational boundary and discretized based on Zhong’s [1] high-order finite-difference shock-fitting method. The unsteady flow over flat plate is excited by a narrow blowing and suction slot composed of 15 different frequencies mounted near the leading edge. Several multi-dimensional cases are tested to demonstrate the order of accuracy for these numerical methods.

5.2 High-Order Cut-Cell Method

Our high-order cut-cell method is presented in this section for the numerical simulation of hypersonic boundary-layer transition with arbitrary surface roughness. The traditional numerical methods of choice for the DNS of transitional and turbulent flows have been spectral methods because of their high accuracies [57-59]. But the applications of spectral methods have been limited to flows in simple domains. Finite-difference methods have recently received much attention for the DNS of transitional and turbulent flows, especially compressible flows, [29, 60-63] because they can be easily applied to complex geometries. High-order schemes are required because traditional second-order schemes do not provide adequate accuracy level for the direct numerical simulation. Most high-order finite-difference methods used in direct numerical simulation are central difference schemes [29, 63] which introduce only phase errors but no dissipative errors in numerical solutions. The shortfall of central schemes is that they are often not robust enough in convection dominated hypersonic flow simulations. On the other hand, Rai et al. [60] show that upwind-bias schemes are very robust in hypersonic flow simulation even when they are made high-order accurate. They use a spatially fifth-order upwind finite-difference scheme in an upwind-bias stencil to compute the Navier–Stokes equations. The numerical dissipation in the upwind-bias schemes is enough to control the aliasing errors and could maintain the overall stability of the method.[64]

5.2.1 Computational Grids and Classification of Grid Points

A schematic of a computational domain and a cut-cell grid in roughness induced hypersonic boundary layer transition is shown in Fig. 11. This figure shows a typical hypersonic flow over a blunt body, where a bow shock is created by the supersonic freestream. In this paper, a high-order shock-fitting method is used to track the movement of the bow shock which is treated as the upper boundary of the computational domain. The computational grid for a shock fitting formulation is bounded between the bow shock above and the blunt body below.

The cut-cell grid is a smooth curvilinear grid fitted to the baseline body shape without the roughness. As a result, the roughness surface cuts across the grid lines. The roughness surface, Γ , is represented by surface equation in the following form,

$$\Gamma : f(x, y, z) = 0 \quad (1)$$

For a problem concerning practical arbitrary roughness in hypersonic vehicle surface, it is likely that there is not an analytical equation applicable to represent the shape of the roughness element. In this case, a set of n discrete coordinate points $\{(x_1, y_1, z_1), (x_2, y_2, z_2), \dots, (x_n, y_n, z_n)\}$ along the physical roughness surface are used to represent the surface. With these roughness data, we can reconstruct the roughness surface for simulation by using a high-order piecewise polynomial interpolation.

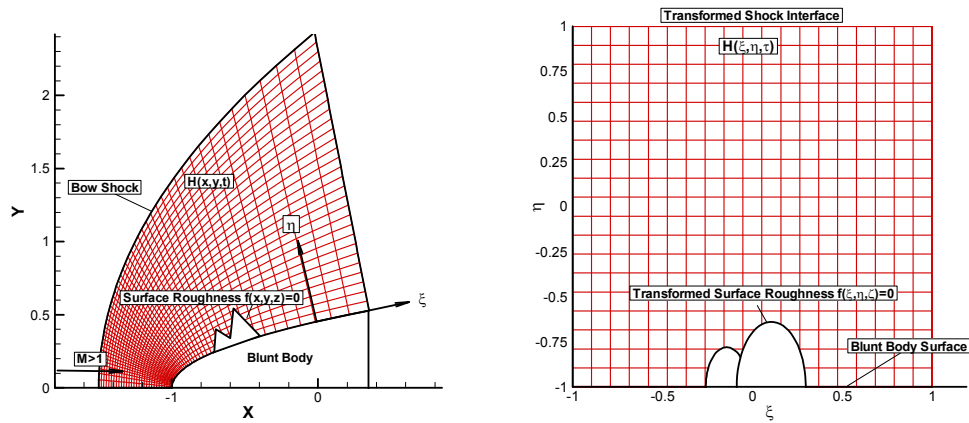


Fig. 11. Physical and computational domain and a cut-cell grid of hypersonic flow over a blunt body with surface roughness: 1) physical grid, 2) computational grid with a transformed roughness.

Both the governing Equation and the roughness equation (1) in the physical domain are transformed into a Cartesian computational domain bounded by bow shock and flat plate boundary. Under the computational coordinate system, the body fitted grids are represented by a curvilinear

three-dimensional coordinates (ξ, η, ζ, τ) along the grid lines. The unsteady movement of the bow shock is treated as the computational upper boundary located at $\eta = \eta_{\max}$, which is time dependent. The other grid lines $\xi = \text{const}$ and $\zeta = \text{const}$ remains stationary during computations. The coordinate transformation is defined by:

$$\begin{cases} \xi = \xi(x, y, z) \\ \eta = \eta(x, y, z, t) \\ \zeta = \zeta(x, y, z) \\ \tau = t \end{cases} \leftrightarrow \begin{cases} x = x(\xi, \eta, \zeta, \tau) \\ y = y(\xi, \eta, \zeta, \tau) \\ z = z(\xi, \eta, \zeta, \tau) \\ t = \tau \end{cases} \quad (2)$$

where (x, y, z, t) are the physical coordinates defined under Cartesian coordinate system.

Substituting Eq. (2) into the governing N-S equation, we obtain a system of transformed governing equations in the computational domain (ξ, η, ζ, τ) as

$$\frac{1}{J} \frac{\partial U}{\partial \tau} + \frac{\partial E'}{\partial \xi} + \frac{\partial F'}{\partial \eta} + \frac{\partial G'}{\partial \zeta} + \frac{\partial E_v'}{\partial \xi} + \frac{\partial F_v'}{\partial \eta} + \frac{\partial G_v'}{\partial \zeta} + U \frac{\partial(1/J)}{\partial \tau} = 0 \quad (3)$$

The transformed fluxes of the equation above are:

$$E' = \frac{F_1 \xi_x + F_2 \xi_y + F_3 \xi_z}{J} \quad (4)$$

$$F' = \frac{F_1 \eta_x + F_2 \eta_y + F_3 \eta_z + U \eta_t}{J} \quad (5)$$

$$G' = \frac{F_1 \zeta_x + F_2 \zeta_y + F_3 \zeta_z}{J} \quad (6)$$

$$E_v' = \frac{F_{v1} \xi_x + F_{v2} \xi_y + F_{v3} \xi_z}{J} \quad (7)$$

$$F_v' = \frac{F_{v1} \eta_x + F_{v2} \eta_y + F_{v3} \eta_z}{J} \quad (8)$$

$$G_v' = \frac{F_{v1}\zeta_x + F_{v2}\zeta_y + F_{v3}\zeta_z}{J} \quad (9)$$

Where $\xi_x, \xi_y, \xi_z, \eta_x, \eta_y, \eta_z, \varsigma_x, \varsigma_y, \varsigma_z$ are transformation metrics, and J is Jacobean matrix of coordinate transformation defined by

$$J = \frac{\partial(\xi, \eta, \varsigma)}{\partial(x, y, z)} \quad (10)$$

In addition to the transformation of the governing equations, the equation for the surface roughness is also transformed into the computational domain and can be represented as

$$f(\xi(x, y, z), \eta(x, y, z, t), \varsigma(x, y, z)) = 0 \quad (11)$$

The grids transformation metrics and the Jacobean matrix J can be obtained either by analytical formulas of the coordinate transformation or by numerical approximation.

With the coordinate transformation, a set of uniformly distributed Cartesian grids can be generated in the computational domain where the grid distribution in the physical domain is not uniformly distributed. Because smooth body-fitted grids are generated in the regular computational domain without the roughness as shown in Fig. 11 (b), some of the Cartesian grid cells may be cut by the roughness boundary, which leads to irregular Cartesian grid cells.

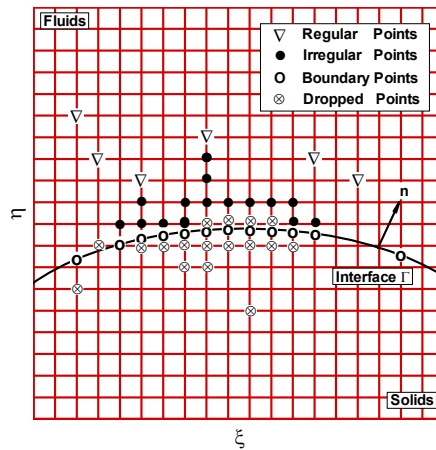


Fig. 12. Classification of four types of grids for the high-order cut-cell method in computational domain (ξ, η) ,

where ∇ represents regular point, \otimes dropped point, \circ boundary point, and \bullet irregular point.

In the current high-order cut-cell finite-difference method, four different types of grid points are defined according to their relative locations with respect to the roughness surface. Different numerical algorithms are implemented for different types of points. The four types of points, as shown in **Error! Reference source not found.12**, are defined as:

- **Boundary points.** The points created by the intersection of roughness interface Γ and grid lines are boundary points. They are not part of the original Cartesian grid, and they are used in finite difference formulas for grid points adjacent to the roughness surface.
- **Irregular points:** For those points located close enough to the roughness boundary Γ that their finite difference stencils contain a boundary point, they are defined as irregular points. In the finite difference approximation involving an irregular point, local grid spacing becomes non-uniform because of the inclusion of a boundary point in the stencil.
- **Dropped points.** If a grid point is adjacent to a boundary point along a grid line with a distance smaller than a pre-specified critical ratio Θ in the ξ or η direction, it is defined as a dropped point along that direction. A dropped point is removed from the grid stencil in the formulation of a local finite difference approximation in the corresponding direction. It should be noted that a grid point can be a drop point in one direction, but a regular point in another direction. Therefore, dropped points are removed in the “dropped direction” only. The same points may be included in finite difference stencils in the other directions if these points are not defined as “dropped”. The value of non-dimensional critical ratio Θ is an adjustable parameter. In the cases of third and fourth order methods, Θ is selected to be 0.5 and 1.0 respectively. All of the points on the solid side of the computational domain are defined as dropped points as well. They do not participate in any numerical calculation.
- **Regular points:** All other grid points produced by the intersection of grid lines themselves are defined as regular points. Since they are relatively far away from boundary points, a standard finite difference approach in a uniform grid can be applied.

5.2.2. Finite-Difference Algorithms for Different Types of Grid Points

The derivatives of the flux terms in Eq. (3) are discretized by different methods for the four different types of grid points. The flux terms in regular points are computed by the standard upwind finite difference scheme introduced in next section. To calculate the flux in irregular points, a high-order non-uniform-grid finite difference method, the stencil of which consists of regular, irregular and boundary points. The dropped points shown in **Error! Reference source not found.12** are not included in non-uniform or uniform grid stencils for computing flux terms in a “dropped” direction. The main purpose of defining a dropped point is to avoid the small cell problem introduced in Section 1. The removal of drop points from finite difference formulas ensures that the distance between two adjacent grid points in a finite-difference stencil is large

enough in order to prevent from the deterioration of corresponding high-order method for computing the hyperbolic part of Eq. (3). Based on the different grid classifications in the computational domain, the details of the different discretization methods for the four types of points are described as follows.

5.2.2.1 Regular points and shock-fitting methods

Since regular points are not affected by the presence of roughness boundary, regular high-order upwind schemes of Zhong [1] are used for the discretization of the governing equations for these points. In addition, the bow shock shown in Fig. 11 is treated by a high-order shock-fitting approach. The finite difference methods and formulas used for the regular points and the bow shock are briefly described here. More details can be found in Zhong [1].

5.2.2.2. Irregular points

Contrary to the standard fifth-order finite-difference schemes used for regular points, special treatment is needed in the discretization of the governing equations for the irregular points because boundary points are included into the finite difference stencil. Fig. 13 shows a schematic of a grid stencil for irregular points near the boundary. In this figure, grid points ξ_2 and ξ_3 are irregular points, ξ_1 is a boundary point, while the grid point between ξ_1 and ξ_2 is a dropped point because it is too close the boundary point. The dropped point is removed from the stencil for the irregular point schemes. The rest of the grid points are regular points. For example, for a local third-order finite-difference approximation at the irregular point ξ_2 , the grid stencil consists of the following five grid points: $\xi_1, \xi_2, \dots, \xi_5$. The grid spacing between the points involved are not uniform because

$$\sigma = \frac{\theta}{\Delta h} \neq 1 \quad (12)$$

where θ is the spacing between ξ_1 and ξ_2 , and Δh is the uniform grid spacing of the regular grid. Therefore, a non-uniform-grid finite difference schemes are needed for irregular points.

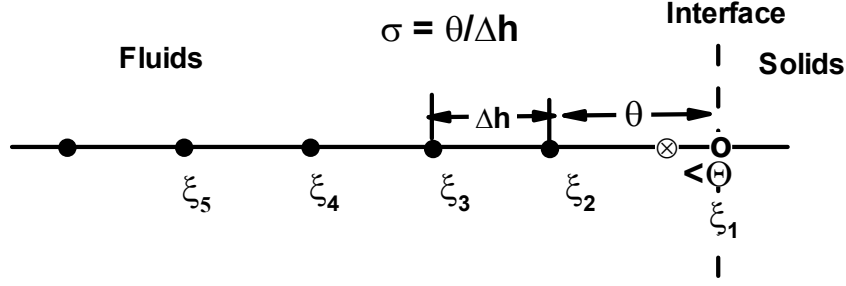


Fig. 13. A schematic of a grid stencil for an irregular point with $p=3$, $q=5$ and $\Omega_3^\xi = \{\xi_2, \xi_3\}$, θ is non-uniform grid spacing after removing a dropped point, Δh is the normal grid spacing, \otimes represents the dropped point, \circ represents the boundary point, and \bullet represents irregular and regular points.

It is assumed that p is the local order of accuracy in boundary of the simulation. In order to maintain a $(p+1)$ -th order global accuracy for the discretization of both the inviscid and viscous flux terms, all local non-uniform schemes for irregular points need to be at least p -th order accuracy. In our construction of high-order cut-cell scheme, if a grid stencil with a number of q grids is used for discretizing regular points near the boundary in each direction of the computational domain, there are $\lfloor q/2 \rfloor$ irregular points near a boundary surface. We denote the collection of all irregular points near this boundary in one direction as set Ω_p^ξ , where the superscript represents the direction of the stencil and the subscript represents the local order of schemes at this point.

As a general convention, the boundary point is labeled as ξ_1 , the irregular points are labeled as $\xi_2, \xi_3, \dots, \xi_{\lfloor q/2 \rfloor + 1}$ sequentially in the order of their distances from the boundary point. A special case with $p=3$ and $q=5$ is shown in Fig. 13. There may or may not be a drop point in the stencil for an irregular point depending on the spacing between the boundary point and its closet regular grid point. As discussed earlier in this paper, if the non-dimensionalized grid spacing between the dropped point \otimes and the boundary point \circ is less than a pre-described critical ratio Θ , this dropped point is removed from the grid stencil in corresponding direction. Otherwise, there is no dropped point in the stencil.

Finite difference formulas for viscous flux terms in irregular points

The discretization of viscous term F_v for an irregular point involves the calculations of second order derivatives since F_v contains gradient terms, such as $\nabla \bar{u}$ and ∇T . Under the coordinate transformation of Eq. (2), $\nabla \bar{u}$ and ∇T can be expressed as derivatives with respect to coordinates in the computational domain (ξ, η, ζ, τ) . A two-step algorithm is employed for the computations of viscous fluxes. First, the gradient of velocity and temperature $\nabla \bar{u}$ and ∇T is computed at each grid point. Using these results, the values of flux vector F_v is evaluated at all grid points. Second, the derivatives of F_v are computed by a finite difference scheme. Since the computations in both steps involve only calculations of first-order derivatives, the same high-order finite-difference schemes are used at each step. In order to do this, the first derivative has to be computed at the boundary points. For boundary points with regular finite-difference stencil, the first-derivative can be calculated by using one-side finite-difference scheme, e.g. for 4th order simulation:

$$(u_x)_1 = \frac{4u_2 - 6u_3 + 4u_4 + u_5}{\Delta h} \quad (12)$$

For boundary points with irregular finite-difference stencil, the first-derivative can be evaluated by using non-uniform one-side finite-difference scheme. The derivation details can follow the following steps.

The general formulation of a non-uniform-grid finite-difference scheme for computing the viscous terms for an irregular point ξ_i of Ω_p^ξ can be written in the following form:

$$\left(\frac{\partial F_v'}{\partial \xi} \right)_i = \frac{1}{\Delta h} \sum_{k=1}^q a_{i,k}(\sigma) F_{v,k}' - \frac{C(\Delta h)^{q-1}}{q!} \left(\frac{\partial F_v'}{\partial \xi} \right)_i^{q-1} \quad \text{for } \xi_i \in \Omega_p^\xi \text{ where } i = 2, 3, \dots, \lfloor q/2 \rfloor + 1 \quad (13)$$

The subscripts of coefficient $a_{i,k}$ stand for the k -th coefficient for the i -th irregular point as defined for the case of $p=3$ and $q=5$ (Fig. 13). The coefficient $a_{i,k}$ is function of σ , which is defined in Eq. (12), and C is a constant.

The coefficients of non-uniform-grid finite-difference equation (Eq. (13)) for every i -th irregular grid point in set Ω_p^ξ can be derived either by a Taylor series expansion, or by taking a derivative of a polynomial interpolated through the non-uniform stencil. We use polynomial interpolation in this paper. Specifically, for each irregular point, the Lagrange interpolation polynomial can be written as

$$\tilde{P}_{q-1}(\xi) = \sum_{l=1}^q \left(\prod_{m=1, m \neq l}^q \frac{\xi - \xi_l}{\xi_l - \xi_m} \right) F'_{v,l} \quad (14)$$

where $\tilde{P}_{q-1}(\xi)$ is a polynomial interpolating through the grid stencil. Differentiating Eq. (14) once with respect to ξ , we have

$$\frac{\partial F'_v}{\partial \xi} \approx \frac{\partial \tilde{P}_{q-1}(\xi)}{\partial \xi} = \sum_{l=1}^q \left(\sum_{n=1, n \neq l}^q \left(\prod_{m=1, m \neq l, m \neq n}^q \frac{\xi - \xi_m}{\xi_l - \xi_m} \right) \frac{1}{\xi_l - \xi_n} \right) F'_{v,l} \quad (15)$$

Substituting $\xi = \xi_i$ into the equation above and comparing terms with those of Eq. (13), we obtain the coefficients $a_{i,k}$ as follows

$$a_{i,k} = \sum_{n=1, n \neq k}^q \left(\prod_{m=1, m \neq k, m \neq n}^q \frac{\xi_i - \xi_m}{\xi_k - \xi_m} \right) \frac{1}{\xi_k - \xi_n} \quad \text{for } k = 1, 2..q \quad (16)$$

where $a_{i,k}$ is a function of σ defined in Eq. (12). In a shock-fitting calculation, the computational grid changes with the movement of the bow shock. As a result, the value of θ is a function of time because of the shock movement.

During the time advancement in the simulation, the grid metrics in the computational domain bounded by the moving shock vary from one time step to the next. As a result, the σ values are not constant. Thus we need to recalculate the finite-difference coefficients $a_{i,k}$ for all irregular points in each time step. In our simulation, the formulas for the coefficients are stored in the computer memory, and their values are computed explicitly when the finite-difference schemes are implemented in each direction.

Finite difference formulas for inviscid flux terms in irregular points

Similar to the local algorithms for the viscous terms at irregular points, a non-uniform-grid high-order upwind scheme is used to discretize the inviscid fluxes, F^{*+} and F^{*-} . For every irregular grid point, there are several possible grid stencils for finite-difference approximation of the flux derivatives of the same accuracy order. Different choices of stencils for these boundary closure schemes lead to different stability characteristics for the overall algorithm. Since F^{*+} and F^{*-} have either all positive or all negative eigenvalues, local grid stencils for finite-difference

approximation of the flux derivatives are chosen so that the discretization for the fluxes are upwind biased, while maintaining high-order accuracy. Therefore, for a given irregular grid point, the stencil for F^{*+} may be different from the stencil for F^{*-} . In addition, a grid stencil for these fluxes may or may not include the boundary point.

The non-uniform-grid finite-difference schemes for the inviscid flux terms of positive and negative eigenvalues can be written as

$$\left(\frac{\partial F^{*+}}{\partial \xi} \right)_i = \frac{1}{\Delta h} \sum_{k=1}^q b_{i,k}^+ F_k^{*+} \quad \text{for } \xi_i \in \Omega_p^\xi \text{ where } i = 2, 3, \dots, \lfloor q/2 \rfloor + 1 \quad (17)$$

$$\left(\frac{\partial F^{*-}}{\partial \xi} \right)_i = \frac{1}{\Delta h} \sum_{k=1}^q b_{i,k}^-(\sigma) F_k^{*-} \quad \text{for } \xi_i \in \Omega_p^\xi \text{ where } i = 2, 3, \dots, \lfloor q/2 \rfloor + 1 \quad (18)$$

The stencil contains a total of q grid points as shown in Fig. 13. The upwind schemes are represented by different sets of coefficients of the two formulas above. Because the upwind bias

stencil used for $\frac{\partial F^{*+}}{\partial \xi}$ does not include the boundary point, the coefficients $b_{i,k}^+$ is not a function

of σ defined in Eq. (12). On the other hand, $b_{i,k}^-$ is a function of σ because the upwind stencil

for $\frac{\partial F^{*-}}{\partial \xi}$ includes the boundary point. The coefficients for each upwind scheme above can be

calculated following the same general formulas given by Eqs. (15) and (16).

The higher-order non-uniform finite-difference stencils require sufficiently many grid points near the roughness surface. When the grids are insufficient for local high-order finite-difference stencil, there are two approaches to overcome the problem. The first approach is to maintain the original number of grids point in the local high-order finite-difference stencil. More grid points can be clustered or generated near the irregular boundary by either adjusting the coordination transformation, or refining the grids in the computational domain. The global grids refinement tends to be very computationally expensive to later simulation. Local grids refinement approach can also be adapted, but extra interpolation procedure has to be implemented for different levels of grids. By generating enough grids points near the irregular interface, the order of accuracy for cut-cell method is maintained. The second approach is to reduce the number of grids in the local finite-difference stencil, where corresponding lower order of non-uniform finite-difference method can be applied. By using this treatment, the local order of accuracy is reduced. If the boundary nearly degenerates, the accuracy of current cut-cell method will not be affected, provided that the boundary interface can be expressed accurately in a numerical or analytical form.

5.2.2.3. Boundary points

As shown in Fig. 11, boundary points are the marker points located at the intersection between the roughness surface and grid lines. The governing equations are not solved at these points. However, flow variables at these points are needed for finite-difference algorithms of the irregular points near the roughness surface. The solid interface imposes the non-slip and non-flow-through conditions for flow velocities at the boundary points. Depending on the actual thermal conditions of the solid surface, either an isothermal or adiabatic wall can be specified. In this paper, only the isothermal wall is considered. In this case, both the velocities and temperature of the boundary points are specified by the wall boundary conditions. The local pressure on the solid surface (boundary points) needs to be computed by the local flow conditions near the wall.

There are several approaches to compute the pressure at the boundary points. One approach is to integrate a local wall-normal momentum equation to obtain the wall pressure. We can also use an approximation assumption of zero pressure gradients at the wall to determine the pressure there. In a previous paper, Zhong used a fifth-order polynomial extrapolation to determine the wall pressure [1]. Satisfactory results have been obtained with this approach. We follow the extrapolation approach of Zhong [1] to determine the pressure at the boundary points.

In computing pressure at the boundary points, the polynomial extrapolation is required to have comparable order of accuracy as that of the interior schemes in order to maintain the expected global accuracy. To maintain a $(p+1)$ -th order global accuracy of the upwind schemes developed in the last sections, it is desirable to have at least p -th order of accuracy for the extrapolation for the boundary points.

Since a boundary point is formed by the intersection of the roughness interface with one of the grid lines, the extrapolation is conducted along the direction of the same grid line. We use the grid line along the ξ direction as an example. The methods can be applied the other directions similarly. In two and three-dimensional cases, there is options of either constructing the extrapolation along the direction normal to the solid interface, or doing it along the grid lines. Though either method can be used in multi-dimensional problems, the latter approach is used in this paper since it is simpler in implementation and more stable for simulations of current tests. In this case, the determination of pressure at the boundary points is a one-dimensional extrapolation along one of the grid lines. The one-dimensional stencil of Fig. 13, which involves non-uniform grid spacing θ , is used to derive the extrapolation formulas for the pressure at the boundary point. For example, for the case of four point extrapolation shown in Fig. 13, pressure at the boundary point $p(\xi_1)$ is obtained by a third degree polynomial interpolating through the following four interior pressures: $p(\xi_2)$, $p(\xi_3)$, $p(\xi_4)$, and $p(\xi_5)$. The grid spacing between neighboring grid points is a constant value of Δh ,

with the exception that the distance between the first and second points are θ . If there is a dropped point in the stencil, the dropped point is not used in the extrapolation calculations.

For two-dimensional problems, the high-order extrapolation along the ξ or η direction is employed to extrapolate pressure from the interior domain into the boundary. A total of p grid points in the direction associated with the boundary point are chosen to be included in the extrapolation stencil. Again, dropped points are not included in the extrapolation stencil. This procedure can prevent the small cell problem of producing numerical instability near the solid boundary.

5.2.2.4. Dropped points

In this paper, in order to avoid the small cell problem, a grid point is designated as a dropped point if its distance from a neighboring boundary point along a grid line is smaller than a pre-determined value Θ . The dropped point, which is associated with a grid direction, is removed in the finite-difference grid stencil along the grid line for the irregular points near the boundary. On the other hand, a grid point may become a dropped point in one direction, but remain a regular or irregular point in another. For example, point P_1 in Fig. 14 is a dropped point in the ξ direction, but a regular point in the η direction. In this case, the flow variables at point P_1 are not used in finite difference formulas for derivatives in the ξ direction. However, the flow variables at the same grid point are needed for finite difference formulas for derivatives in the η direction. The flow variables at this dropped point P_1 are obtained by the interpolation of a stencil along the ξ direction.

For a grid point which is a regular or irregular point in one direction, but a dropped point in another, finite difference schemes along the former direction may include this point in its stencil. As shown in Fig. 14 for the case of $p=3$, the finite-difference stencil for an irregular point Q located at (ξ_i, η_j) contains five points in the η direction, which are in set $\Omega_Q = \{(\xi_i, \eta_{j+2}), (\xi_i, \eta_{j+1}), (\xi_i, \eta_j), (\xi_i, \eta_{j-1}), (\xi_i, \eta_{j-2})\}$. There are two dropped points along the ξ direction in this set of stencil Ω_Q : point P_1 at (ξ_i, η_{j-1}) and point P_2 at (ξ_i, η_{j-2}) . If the points P_1 and P_2 are removed from the stencil used in the calculations of flux terms $\partial F' / \partial \eta$ and $\partial F'_v / \partial \eta$ in Q , the stencil set Ω_Q needs to be shifted two grids down to include

(ξ_i, η_{j-3}) and (ξ_i, η_{j-4}) to maintain the accuracy. In this case, the resulting stencil for Q may contain a significantly large interval θ compared with the normal grid spacing Δh , which may lead to a deterioration of accuracy of the method. Therefore, we maintain the original grid stencil Ω_Q , which includes points P_1 and P_2 , along the η direction for point Q . We calculate the flow variables of these two dropped points by interpolation along the ξ direction.

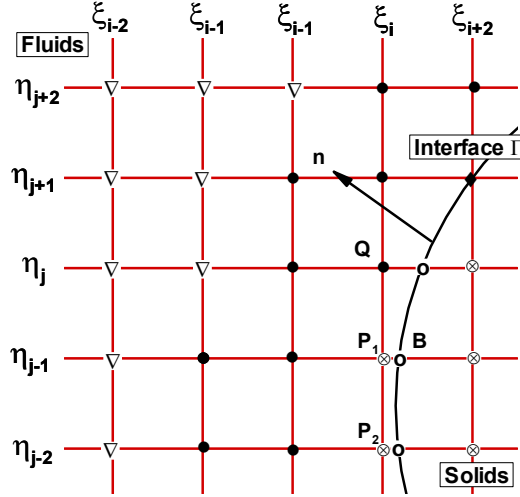


Fig. 14. An example of a grid point, such as point P_1 and point P_2 , which is a regular or irregular point in one direction, but a dropped point in another for the case of $p=3$: ∇ represents regular points, \otimes dropped points, O boundary points, and \bullet irregular points.

For the case of $p=3$ for point P_1 , a third-order polynomial interpolation along the ξ direction is employed to compute the flow variables at this point. The interpolation is carried out along the ξ direction, which is along the direction where the point is dropped. For $p=3$ as shown in Fig. 14, the interpolation stencil for point P_1 is set $\Omega_p = \{(\xi_{i-1}, \eta_{j-1}), (\xi_{i-2}, \eta_{j-1}), B\}$, where B represents the boundary point. For higher order method, the order of interpolation needs to be increased accordingly. For $p=4$, a fourth order interpolation should be used. For a general case of p -th order methods at the boundary, a total of $p-1$ adjacent grid points and exactly one boundary point along the ξ direction are chosen as the interpolation stencil. The interpolant can

be written as

$$\tilde{U}(\xi_{p_1}) = \sum_{n=1}^p \left(\prod_{l=1, l \neq n}^p \frac{\xi_{p_1} - \xi_l}{\xi_n - \xi_l} \right) U_n \quad (19)$$

Where ξ_{p_1} is the ξ coordinate of dropped point, $\{U_i, i=1..p\}$ is conservative flow variables at the grid points of the interpolation stencil.

Similar interpolation procedures can also be carried out if a point is designated as a dropped point in the η direction, but is an irregular or regular point in the ξ direction. If a grid point is designated as a dropped point in both the ξ and η directions, there is no need to do interpolations because this point is removed from the calculations of both directions.

5.3 Test and applications

The new high-order cut-cell method has been tested in the computations of several one and two-dimensional hyperbolic and elliptic equation in irregular domains. The results show that up to fourth-order accuracy in both L^2 and L^∞ norm can be obtained for the current cut-cell method for both problems. We subsequently have applied a third-order cut-cell method to the two-dimensional compressible Navier-Stokes equations for simulating roughness induced receptivity for hypersonic flow over a flat plate with a blowing and suction slot placed near the leading edge. The surface roughness height is approximately half of the local boundary thickness. By using the uniformly third-order cut-cell method, small disturbances generated by the blowing and suction slot are well resolved around the roughness element. The results obtained by the new third-order cut-cell method are consistent with those of the linear stability analysis results. In addition, steady solutions of the flow affected by the roughness are well captured by the cut-cell method. The simulation results suggest that the existence of small surface roughness ($h = \frac{1}{2}\delta$) affects the propagation of instability waves in the hypersonic boundary layer. The details regarding the tests can be found in [1].

6 STABILIZATION OF A MACH 5.92 FLAT-PLATE BOUNDARY LAYER WITH FINITE HEIGHT SURFACE ROUGHNESS

One of the major accomplishments of the current research project is on revealing the receptivity mechanism of a hypersonic boundary layer with finite surface roughness to wall blowing-suction. These results are discussed in more detail in this section. Details of these results have been published in **Publications:** [3], [9], [13], [15], [20].

6.1 Flow conditions and roughness model

With the development of advanced computers and numerical techniques, numerical simulation of the receptivity process by directly solving Navier-Stokes equations has become feasible. By solving the compressible linearized Navier-Stokes equations, Malik et al. [65] investigated the responses of a Mach 8 flow over a sharp wedge of a half-angle of 5.3° to three types of external forcing: a planar free-stream acoustic wave, a narrow acoustic beam enforced on the bow shock near the leading edge, and a blowing-suction slot on the wedge surface. They concluded that these three types of forcing eventually resulted in the same type of instability waves in the boundary layer. However the receptivity mechanism was not studied in detail. Ma and Zhong [66] studied the receptivity mechanisms of the same hypersonic boundary layer to various freestream disturbances, i.e., fast and slow acoustic waves, vorticity waves, and entropy waves, by solving the two-dimensional compressible Navier-Stokes equations. They found that the stable modes in the boundary layer played a very important role in the receptivity process.

In this report, the new cut-cell method introduced in Section 5 is used to compute hypersonic viscous flow over a flat plate with an isolated surface roughness element (Fig. 1). Both steady and unsteady flows are considered. The freestream flow conditions are the same as those used in Maslov's experiment [13] as follows,

$$\begin{cases} P_r = 0.72, R_\infty = \rho_\infty * u_\infty / \mu_\infty = 1.32 \times 10^6 / m \\ M_\infty = 5.92, T_\infty = 48.69 K, P_\infty = 742.76 Pa \end{cases} \quad (20)$$

where M_∞ , T_∞ , P_∞ , P_r , R_∞ are Mach number, temperature, pressure, Prantle number and unit Reynolds number, respectively. The flat plate is assumed to be isothermal with a constant temperature of $T_w = 350.0 K$. The total length of the flat plate is about 1.69m.

In this section, unless stated otherwise, most flow variables are presented as dimensionless ones. The main exception is that the x and y coordinates are presented in dimensional form so that the simulational results can be easily related to the experimental setup. For other variables, we nondimensionalize the flow velocities by the freestream velocity u_∞ , density by ρ_∞ , pressure by $\rho_\infty (u_\infty)^2$, and temperature by T_∞ .

An isolated roughness element of smooth shape is placed on the surface of the flat plate at $x = 0.185m$ downstream. Motivated by Whitehead's experiments [67], the shape of the surface roughness is chosen to be a two-dimensional bump, governed by the following elliptic equation,

$$\frac{(x-x_c)^2}{a^2} + \frac{y^2}{b^2} = h^2 \quad (21)$$

The computations of this study are performed under the following parameters: $a = 2$, $b = 1$, $x_c = 0.185m$ and $h = \delta/2$ where $\delta = 0.00081m$ which corresponds to the boundary layer thickness at x_c as shown in Fig. 15.

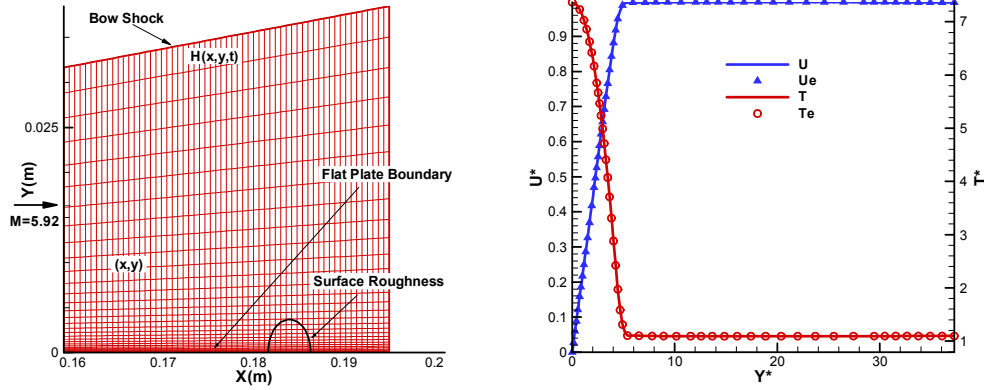


Fig. 15. 1) Computational grid for hypersonic flow over a flat plate with an isolated surface roughness. The grid size is 241×121 (showing one out of four grid points in both directions, 2). Comparison of the current shock-fitting results with theoretical solutions (T_e and u_e) for temperature and wall normal velocity distributions long a wall-normal grid line located at $x = 0.1676m$ on the plate surface.

In this report, a third-order cut-cell method described in Section 5 is used to compute the two-dimensional viscous hypersonic flow over the flat plate with the roughness element. As described in Section 5, a coordinate transformation is employed to transform the physical domain shown in Fig. 15 into a rectangle computational domain with a set of Cartesian grid. The optimal transformation formula is determined by the specific physical problem considered. For viscous flow over a flat plate, it is necessary to cluster more grid points at the bottom wall surface in order to resolve the viscous boundary layer. In this paper, a two-step mapping procedure is used to obtain better resolution inside the viscous boundary layer.

In the first step of the transformation, the entire physical domain shown in Fig. 15 is transformed into a square domain defined on $[0,1] \times [0,1]$ as an intermediate coordinate space. The transformation relation is defined as:

$$\begin{cases} X = \frac{x - x_{start}}{L} \\ Y = \frac{y}{H(x, y)} \end{cases} \quad (22)$$

where (X, Y) is defined under the intermediate coordinate system, L is the streamwise length of the flat plate in physical domain, x_{start} is the streamwise coordinate of starting point of computation in each zone, and the distance along η direction between the solid wall and bow shock is referred to H .

In the second step of the transformation, the intermediate plane in the (X, Y) space is mapped into the final computational domain (ξ, η) in order to cluster more grid points into the viscous boundary layer near the flat plate surface. In the present study, an exponential stretch function is used to cluster grids in the η direction as follows,

$$\begin{cases} X = \xi \\ Y = -\frac{\left(\frac{\beta+1}{\beta-1}\right)^{(1-\eta)} - 1}{\left(\frac{\beta+1}{\beta-1}\right)^{(1-\eta)} + 1} \beta \end{cases} \quad (23)$$

where β is the stretching parameter. The value of $\beta = 1.01$ is used in this paper. With this β value, about 50% of the total grid points in the η direction are clustered inside the boundary layer. The combination of the transformations of these two steps leads to overall transformation given by Eq. (2).

In the computational domain (ξ, η) , the baseline grid is a set of Cartesian grid similar to the schematic shown in Fig. 11 (2). The interaction of the roughness surface with the grid lines creates cut cells, which are treated by the current cut-cell method. The surface equation (21) of the roughness surface is transformed into the computational domain in order to apply the cut-cell method. By substituting Eqs. (22) and (23) into the roughness surface Eq. (21), the analytical

equation for roughness surface in the computational domain can be written as

$$f(\xi, \eta) = \frac{(L\xi)^2}{a^2} + \frac{\ell H(\xi L + x_{start})^2}{b^2} - h^2 = 0$$

$$\text{where } \ell = \frac{\left(\frac{\beta+1}{\beta-1}\right)^{(1-\eta)} - 1}{\left(\frac{\beta+1}{\beta-1}\right)^{(1-\eta)} + 1} \beta \quad (24)$$

From Eq. (24), we can calculate the coordinates of the boundary points by computing the coordinates of the intersection between the roughness surface and the grid lines. For a given value of ξ along the roughness surface, the Newton iteration method is employed to solve Eq. (24) for the corresponding value of η on the surface for a boundary point, and vice versa. Having computed the boundary points, we can identify all irregular and dropped points near the roughness surface. The remaining grid points are regular points.

After computing all coordinates of the irregular, regular, boundary and dropped points as shown in Fig. 11, the current high-order cut-cell method is applied to discretize Eq. (3). The bow shock is treated by a high-order shock-fitting method. The overall accuracy of simulation is determined by the order of scheme used for computing the inviscid and viscous flux terms.

6.2. Steady flow solution without surface roughness

The steady mean flow solutions are calculated by using the fifth-order shock-fitting method. But in the leading edge region of the flat plate, there is a singularity at the tip of the plate and the high-order shock fitting method cannot be used there. Thus a second-order TVD shock-capturing method is employed to calculate a small local flow field around the tip of the flat plate. The computational domain for the TVD calculations starts at $x = -0.006m$ and ends at a very short distance downstream of the leading edge at $x = 0.003m$. A total 241×121 grid points are used. A TVD scheme, which follows that used by Lee et al. [68], is applied to Eq. (3). The semi-discrete system of ordinary differential equations are then solved by using a fourth-order Runge-Kutta method.

Having obtained the steady state solutions at the leading edge, we then use the solution of the TVD scheme as the inlet condition to start the subsequent shock-fitting calculations. The computational domain for the high-order shock-fitting methods starts at $x = 0.003m$ and ends at $x = 1.68784m$. In actual simulations, the computational domain is divided into 30 zones, with total of 5936 grid points in the streamwise direction and 121 points in the wall-normal direction. As mentioned above, the second zone uses the results of the first zone of the second-order TVD solution as the inlet condition. A later zone uses the interpolation of its former zone's data as the inlet condition.

The solutions for the steady viscous flow over the flat plate with no surface roughness are first obtained. Fig. 15 shows the streamwise velocity and temperature profiles along the wall-normal direction at $x = 0.1676m$ near the wall. The current numerical solutions obtained by the fifth-order shock-fitting scheme are compared with the self-similar boundary layer solution. In order to compare with the self-similar solution of the boundary layer, the y coordinate is nondimensionalized by $\sqrt{x\mu_\infty/\rho_\infty u_\infty}$. Fig. 15 illustrates that the results of the current numerical simulation agree very well with the theoretical solutions near the wall. The second-order TVD scheme is accurate enough to be used as the inlet condition of the fifth-order shock-fitting method downstream of the leading edge.

6.3. Steady flow solution with an isolated surface roughness

The roughness model proposed in Sec 6.1 is simulated by using the high-order cut-cell method with same flow condition in Sec 6.2. In this report, the results of a third-order ($p = 3$) cut-cell method is presented. In simulation, the numerical dissipation coefficient α is chosen within range $[0.25 - 6.0]$. All the simulations are very stable. Thus the numerical dissipation of the interior scheme may only have minor influence on the overall stability.

Fig. 16 shows steady flow solutions computed by the third-order cut-cell method, in both the streamline pattern and the contours of wall normal velocity and pressure components. In order to assess the numerical accuracy of the solutions, steady solutions are obtained by using the following two sets of grids: 241×121 and 441×121 . Due to the restriction of computational time, the grid refinement study is only performed with respect to streamwise resolution in one zone. The wall-normal velocities computed by fine and coarse grids are plotted with the same levels of contour line in Fig. 16. The good agreement between these two sets of results suggests that the grid resolution used in the current simulations is high enough for the steady flow simulation. Fig. 16 also shows the steady-flow pressure contours for flow over a flat plate with an isolated roughness computed by the third-order cut-cell method. Because the flow is supersonic behind the bow shock, a family of Mach waves is generated by flow over the roughness. The compression waves are followed by expansion waves when the flow expands around the roughness surface. These Mach waves are approximately parallel to the bow shock interface in the later zones.

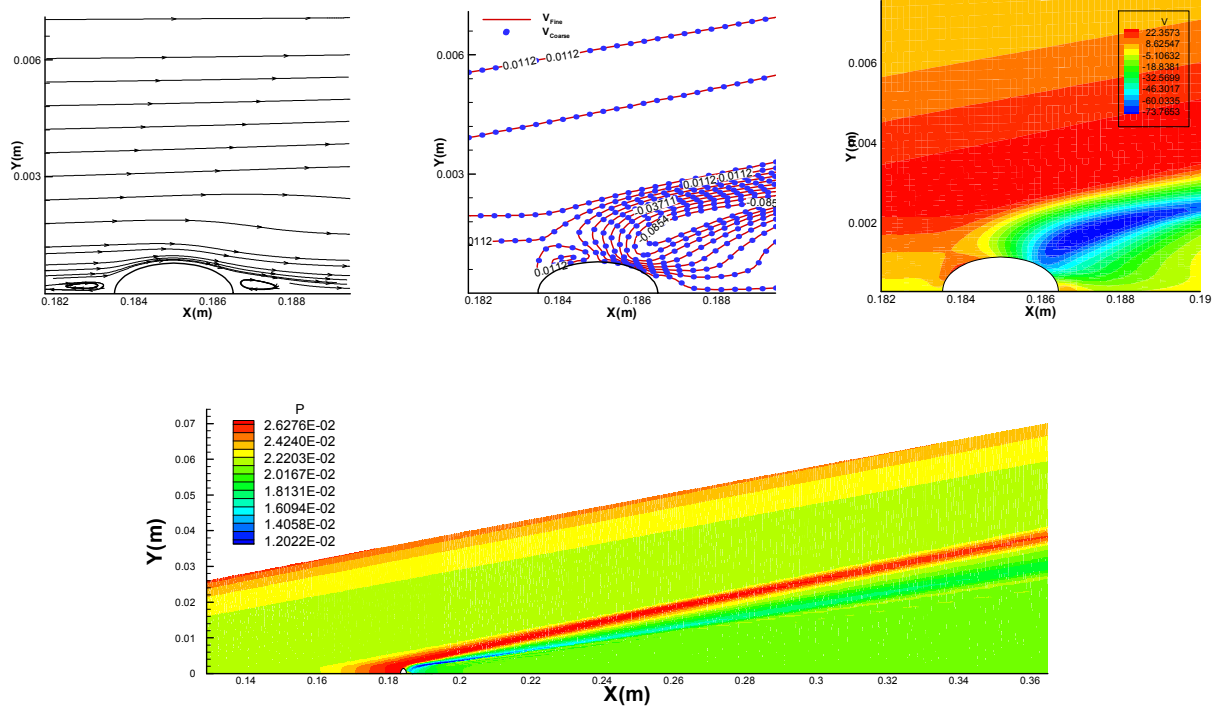


Fig. 16. Hypersonic flow solutions in the region near the roughness element computed by the third-order cut-cell method: 1) streamline pattern, 2) contour lines of wall normal velocity components computed by using two sets of grids (coarse grid: 241×121 , fine grids: 441×121), 3) wall normal velocity contour 4), Pressure contours for two-dimensional hypersonic flow over a flat plate with an isolated roughness computed by the third-order cut-cell method. The total grid points in this range of the flow field is 1920×121 .

The steady flow solutions demonstrate that, affected by the roughness, hypersonic boundary layer over the flat plate is modified significantly in the regions both downstream and upstream of the roughness element. The parallel flow assumption is no longer valid for flow near the roughness. Consequently, normal-mode linear stability analysis may not be accurate in this flow region. Thus a different boundary layer instability mechanism may be introduced. On the other hand, the effects of the roughness is most significant in the regions surrounding the roughness. The roughness effects on the steady flow decay if we move further downstream. Thus the flow is approximately parallel again in the far downstream of the surface roughness. Linear Stability Theory (LST) can be applied to analyze the flow field which is approximately parallel. Good agreement between numerical and theoretical solutions can be achieved. More details can be found in [69].

6.4. Receptivity of hypersonic flow with surface roughness to wall blowing and suction

In this section, the new third-order cut-cell method is applied to the computation of transient responses of the same Mach 5.92 boundary layer to forcing waves introduced by a blowing and

suction slot located on the plate surface. It is termed the receptivity problem of the boundary layer to forcing waves [24]. The receptivity problem is critical to the understanding of physical mechanisms of hypersonic boundary layer transition. The receptivity of the same hypersonic boundary layer to wall blowing and suction has been studied by Wang and Zhong [70] and [71] for smooth surface without roughness. In this paper, we study the additional effects of the isolated surface roughness on the receptivity process by using the current third-order cut-cell method. The current results are compared with those of [70] and [71] to study the effects of surface roughness on the receptivity process.

The receptivity study is mainly concerned with the excitation of instability waves, the characteristics of which can be analyzed by the linear stability theory [72]. The instability theory analyzes the propagation of individual sinusoidal waves in the streamwise direction inside the boundary layer. These waves are referred as Tollmien-Schlichting (T-S) waves for low speed flow. The instability waves are vorticity waves, whose amplitudes vary though the boundary layer and die off exponentially outside the boundary layer. For the case of small perturbations in the flow field, the perturbations of flow variables can be written in the form of a normal mode, i.e.,

$$\begin{pmatrix} u \\ v \\ w \\ p \\ \theta \end{pmatrix} = \begin{pmatrix} \tilde{u}(y) \\ \tilde{v}(y) \\ \tilde{w}(y) \\ \tilde{p}(y) \\ \tilde{\theta}(y) \end{pmatrix} e^{i(\int \alpha dx + \beta dz - \omega t)} \quad (25)$$

where θ is the perturbation of temperature. The frequency of the waves is ω and the streamwise and spanwise wave numbers of the instability wave are represented by α , and β respectively.

Substituting Eq. (25) into a linearized version of the full Navier-Stokes, we obtain a system of linearized equations of the stability theory. These equations are required to satisfy a number of boundary conditions. By imposing the homogenous physical conditions, the number of solutions of an eigen problem to the linearized equations with specific value of α, β and W is constrained.

The relation for the instability wave parameter α, β and W are referred as dispersion relations in the following form,

$$W = W(\alpha, \beta) \quad (26)$$

Extensive numerical and theoretical research has been conducted to solve the linearized Navier-Stokes equations and many characteristics regarding the instability waves in hypersonic boundary layers have been discovered. [13, 72-75]. Mack [72] identified the unstable modes by

using the linear stability theory. He showed that inside a supersonic boundary layer, there are multiple higher instability modes in addition to the first mode, which is the compressible counterpart of T-S waves in the incompressible boundary layers. These instability modes in the supersonic boundary layer are termed as first mode, second mode, third mode, etc. The second mode is also called the Mack mode. For supersonic boundary layer with Mach number larger than four, the second Mack mode is the most unstable mode, and it plays an important role in hypersonic boundary layer transition.

To excite the propagation of small disturbances inside the boundary layer, a blowing and suction slot is imposed as periodic-in-time boundary conditions for the perturbations of the mass flux on the wall. The blow-suction slot is located at $x = 0.030m$ and spreads over several grids spaces. The perturbations in the blowing and suction slot are governed by the following function:

$$\rho v = q_0 g(l) \sum_{n=1}^{15} \sin(w_n t) \quad (27)$$

where q_0 is an amplitude parameter, $w_n = n f_1$ is circular frequency of this multi-frequency perturbation, and $g(l)$ is a non-dimensional x-direction profile function defined as

$$g(l) = \begin{cases} 20.24l^5 - 35.4375l^4 + 15.1875l^3 & (l < 1) \\ -20.24(2-l)^5 + 35.4375(2-l)^4 - 15.1875(2-l)^3 & (l \geq 1) \end{cases} \quad (28)$$

The variable l is the non-dimensional parameter associated with current coordinate of this blowing and suction,

$$l(x) = \frac{2(x - x_i)}{(x_e - x_i)} \quad (29)$$

he basic frequency f_1 is given by $f_1 = 50kHz$, and the other 14 different frequencies are imposed as $f = 100, 150, 200 \dots kHz$ for $n = 2, 3, 4, \dots$. This steady and unsteady flow conditions used in the current simulation are the same as those used in the simulation conducted by Wang et al. [70] for the cases of smooth wall without roughness. Balakumar [76] also investigated the receptivity of a 2-D roughness to acoustic waves and found the isolated roughness does not contribute much in generating unstable disturbances.

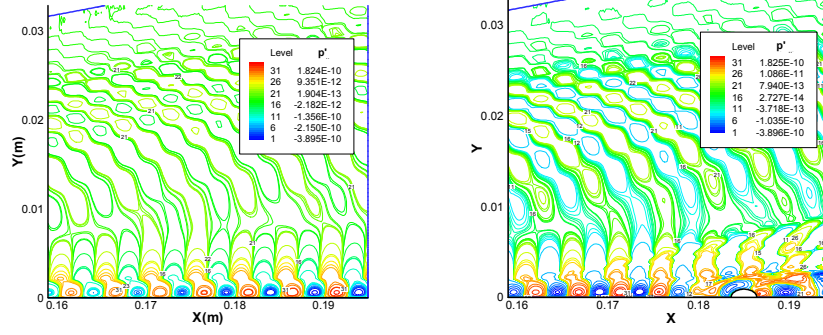


Fig. 17. Comparison of contours of pressure perturbations for unsteady Mach 5.92 flow over a flat plate with and without surface roughness. The forcing frequency is $f = 150kHz$. The current results for flow without 1), or with 2) roughness are computed by the third-order cut-cell method.

The simulation is carried out with combined forcing waves of fifteen frequencies. A Fast Fourier Transformation (FFT) technique is used to separate the results with different frequencies. Fig. 17 compares the contours of pressure perturbations for unsteady Mach 5.92 flow over a flat plate with and without surface roughness. The forcing frequency is $f = 150kHz$. The current results for flow with roughness are computed by the third-order cut-cell method. The corresponding results for the smooth surface without roughness was obtained by Wang and Zhong [70] and [71]. Fig. 17 (1) shows that, for the case of no surface roughness, instability waves, which are induced by the forcing waves introduced at the blowing and suction slot, propagate downstream in the streamwise direction inside the boundary layer. Fig. 17 (2) shows how the roughness element interacts with the wave propagation inside the boundary layer.

Fig. 18 compares the contours of pressure perturbations for cases with and without surface roughness for a longer flow region with combined 15 forcing frequencies. The roughness is located at $x_c = 0.185m$. The pressure disturbances at flat plate surface are reduced significantly after the instability waves pass the surface of roughness element. Thus the local surface roughness could potentially stabilize the instability waves in the boundary layer.

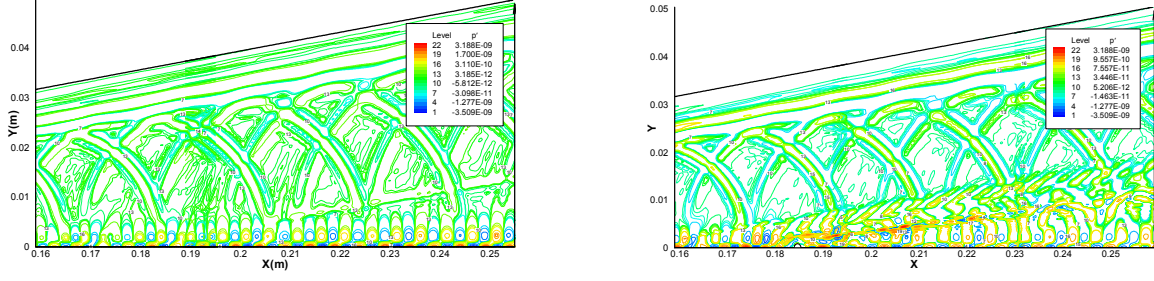


Fig. 18. Comparison of contours of pressure perturbations for unsteady Mach 5.92 flow over a flat plate with and without surface roughness for a longer flow region. The forcing frequency is combined 15 frequencies.

The roughness is located at $x_c = 0.185m$.

A multi-domain spectral collocation (MDSC) method of Malik [77] is used to conduct stability analysis of the steady solution for the hypersonic flow over the roughness element. More details about the linear stability analysis and methods can be found in [77].

The dimensionless frequency used for linear stability analysis is defined as

$$F = \frac{2\pi f\nu}{u_\infty^2} \quad (30)$$

where F is dimensionless frequency, ν is kinematic viscous coefficient. In present simulation, $\nu = 6.05 \times 10^{-5} m^2/s$, $F = 5.30 \times 10^{-5}$ for the case of $f = 100kHz$ and $u_\infty = 827.29m/s$.

In LST analyses of boundary layer flows, the Reynolds number based on the local length scale of boundary layer thickness, δ , is generally used. They are expressed as

$$R = \frac{\rho_\infty u_\infty \delta}{\mu_\infty}, \delta = \sqrt{\frac{\mu_\infty x}{\rho_\infty u_\infty}} \quad (31)$$

Hence the relation between the R and the unite Reynolds number R_∞ is,

$$R = \sqrt{R_\infty x} \quad (32)$$

With the definitions of Reynolds number R and the dimensionless frequency F , the dimensionless circular frequency ω can also be expressed as

$$\omega = RF \quad (33)$$

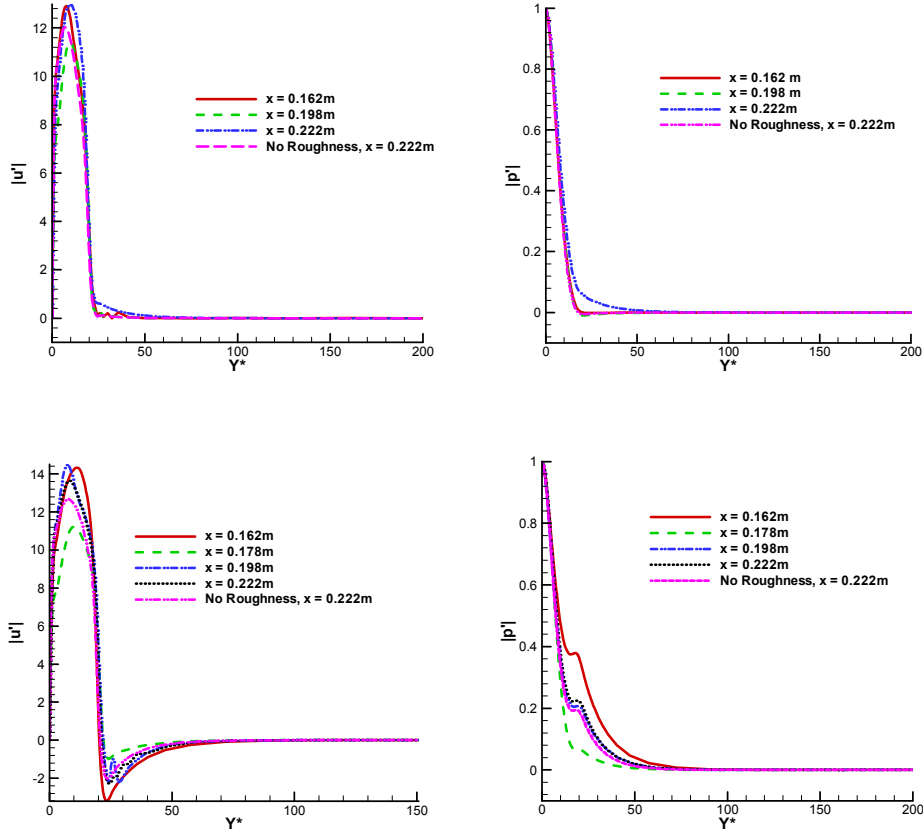


Fig. 19. Wave mode profiles obtained by linear stability analysis at various locations: 1) mode F profile for velocity, 2) mode F profile for pressure, 3) mode S profile for velocity, 4) mode S profile for pressure. The amplitudes of disturbances are nondimensionlized by their corresponding values on the surface of flat plate.

There are two major wave modes in hypersonic boundary layers: mode F and mode S. Fig. 19 shows wave mode profiles obtained by linear stability analysis at various locations for both mode F and mode S. The disturbance amplitudes are nondimensionlized by the pressure disturbance on the surface of flat plate, e.g. $u'(y) = \tilde{u}(y) / \tilde{p}(0)$. In the upstream of roughness at $x = 0.1620m$ where the roughness effects on the mean flow are not that significant, mode S and mode F can be indentified clearly. As we move gradually downstream, the profiles of the wave modes vary significantly. After $x = 0.1980m$, mode S and mode F can be identified again by examining their perturbation profiles. The mean flow solution obtained by the cut-cell method can produce accuracy results for the stability analysis.

6.5 Stabilization effect of location of the finite roughness

In order to investigate the effect of location of the finite surface roughness on receptivity and stabilization, a series of numerical simulations have been carried out for different roughness locations. Specifically, four cases of different roughness locations are considered. Fig. 20 shows a schematic of different roughness locations for the four cases. In each case, wall blowing-suction

with fifteen frequencies is introduced on the flat plate surface. The subsequent responses of the boundary layer are simulated by the high-order cut-cell finite difference method.

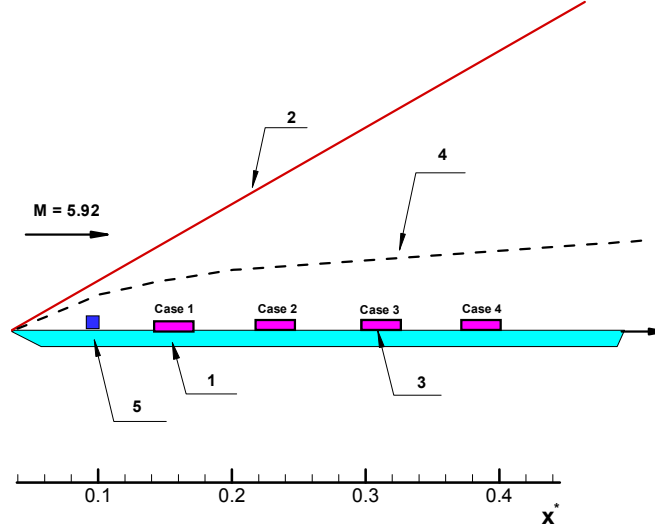


Fig. 20 A schematic of locations of the blowing-suction actuator for the four cases: 1. flat plate; 2. bow shock; 3. surface roughness; 4. boundary layer; 5. blowing suction.

Specifically, roughness locations with respect to the synchronization point at $x = 0.331m$ are as follows,

- **Case 1:** Upstream of the synchronization point $x = 0.185m$; The roughness height $h = \frac{1}{2}\delta = 0.00081m$.
- **Case 2:** Upstream of the synchronization point $x = 0.260m$; The roughness height $h = \frac{1}{2}\delta = 0.00111m$.
- **Case 3:** Synchronization point $x = 0.331m$; The roughness height $h = \frac{1}{2}\delta = 0.00141m$
- **Case 4:** Downstream of the synchronization point $x = 0.410m$; The roughness height $h = \frac{1}{2}\delta = 0.00171m$.

Fig. 21 shows the pressure amplitude on the flat plate surface with roughness located in different locations. It shows that for all four cases, the development of two-dimensional wall perturbations eventually result in the same type of instability wave (mode S) in the boundary layer. When the

surface roughness located in the far upstream of the synchronization point (Case 1), the instability wave develops in the same way as the case without roughness. But as the roughness moves gradually into the downstream (Case 2), the amplitude of pressure in the flat plate surface is amplified. Mode S is destabilized when the roughness element is placed sufficient close to the synchronization point. In Case 3 and Case 4, when the roughness located in downstream of synchronization point, the finite surface roughness stabilizes the unstable wave inside the boundary layer. The amplitude of pressure perturbation is reduced in further downstream.

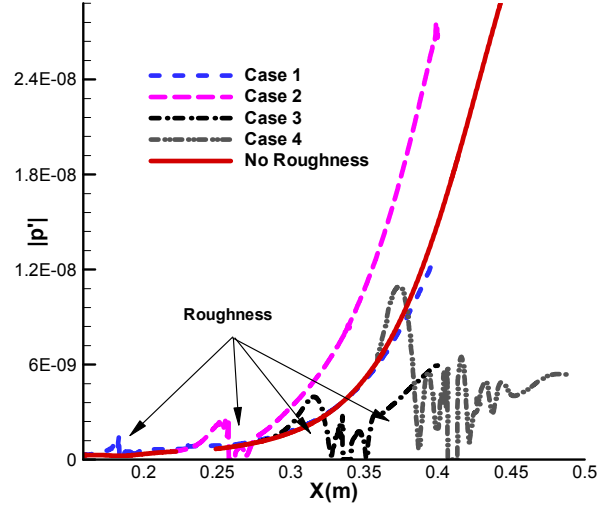


Fig. 21. Numerical simulation of receptivity of the Mach 5.92 flow over a flat plate to two-dimensional wall perturbations with surface roughness: Amplitude comparison of pressure for four cases.

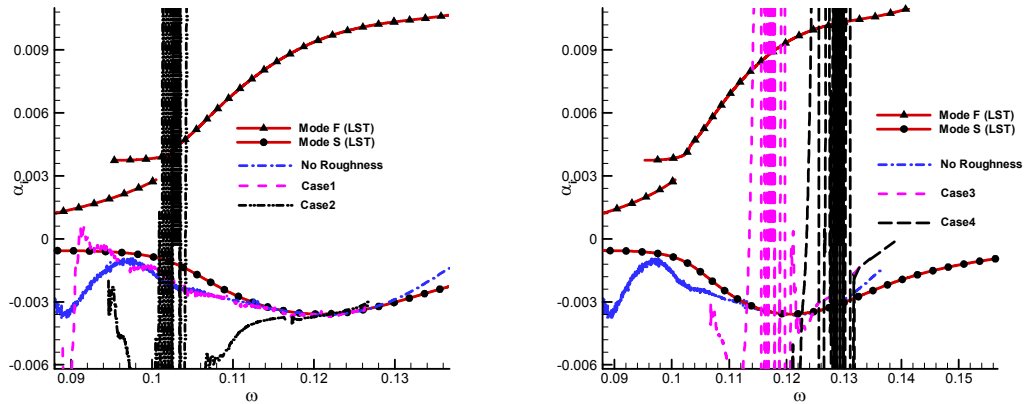


Fig. 22. Numerical simulation of receptivity of the Mach 5.92 flow over a flat plate to two-dimensional wall perturbations with surface roughness: comparison of numerical and LST growth rates.

Fig. 22 shows the comparison of numerical and LST growth rate α_i as variation of dimensionless circular frequency ω . The DNS result and LST does not agree initially due to the existence of various eigen modes perturbations. After $\omega > 0.12$ ($x > 0.33m$), mode S becomes dominant among the eigen modes spectral. Thus after the Mode S fully develops in the boundary layer, the theoretical growth rate α_i of Mode S plotted in red lines agrees well with the DNS result. In the region surrounding the surface roughness element, the pressure perturbation on the plate surface oscillates strongly for all four cases, which drive the growth rate α_i to be infinite. But in the downstream of surface roughness, the mean flow is restored and the Mode S growth rate can be calculated. For Case 1, the growth rate does not change much with the roughness effect. This shows the roughness only affect local mean flow and local mode S instability. But for Case 2, mode S is destabilized before the synchronization point ($\omega \approx 0.12$), and develops in a similar way to case without roughness after that. Thus the modified local mean flow amplifies the amplitude of perturbation. One explanation to this is the non-parallel feature of local mean flow with positive wall-normal velocity. For Case 3 and 4, being very different from Case 1 and 2, mode S is stabilized after the synchronization point. This once again can be explained as the non-parallel feature of the local mean flow with roughness in the upstream and negative wall-normal velocity. More accurate theoretical analysis tools beyond LST should be adopted to analyze this non-parallel region.

To summarize, the current simulation results have indicated that the roughness location plays an important role in the developments of mode S by the blowing-suction actuator. Mode S is destabilized only when the roughness element is located close upstream of the synchronization point. On the other hand, when the roughness element is downstream of the synchronization point, mode S is stabilized. This happens even when the roughness is still within the unstable region of mode S. Therefore, the synchronization point and finite roughness location is critical to the receptivity process. The relationship between the location of the roughness and the synchronization point suggests that, in order to control or delay the laminar-turbulent transition more efficiently, the roughness element should be placed upstream of the synchronization point between mode S and mode F.

7 PERSONNEL

The following personnel conduct research for the grant and are partially supported by the grant:

1. Professor Xiaolin Zhong, principal investigator.
2. Xiaowen Wang, a postdoctoral researcher.
3. Le Duan, a Ph.D. student.

4. Jia Lei, a Ph.D. student.

8 PUBLICATIONS

The following publications are completed from work supported by this grant:

In Journals or Book Chapters:

- 1 L. Duan, X. Wang and X. Zhong, “A High-Order Cut-Cell Method for Numerical Simulation of Hypersonic Boundary-Layer Instability with Surface Roughness” submitted to the **Journal of Computational Physics** for publication, July 2009.
- 2 Wang and X. Zhong, “Receptivity of a Mach 8 flow over a sharp wedge to wall blowing-suction,” accepted to be published at **AIAA Journal**, 2009.
- 3 X. Wang and X. Zhong, “An efficient approach to stabilize a hypersonic boundary layer using porous coating,” accepted to be published at **Physics of Fluids**, 2009.
- 4 Tumin, X. Wang, and X. Zhong, “Direct numerical simulation and theoretical analysis of perturbations in hypersonic boundary layers,” **Proceedings of the seventh IUTAM symposium on laminar-turbulent transition**, Stockholm, Sweden, 2009, edited by P. Schlatter and D. S. Henningson, 2010.
- 5 X. Wang and X. Zhong, “Effect of wall perturbations on the receptivity of a hypersonic boundary layer,” **Physics of Fluids**, 21, 044101 (1-19) 2009.
- 6 X. Wang and X. Zhong, “Receptivity of a Hypersonic Flat-Plate Boundary Layer to Three-Dimensional Surface Roughness,” **Journal of Spacecraft and Rockets**, Vol. 45, No. 6, pp. 1165-1174, November–December 2008.

In Conference Proceedings:

- 7 L. Duan and X. Zhong “A High-Order Cut-Cell Method for Numerical Simulation of Three-Dimensional Hypersonic Boundary-Layer Transition with Finite Surface Roughness”, **AIAA paper 2010-1450**, January 2010.
- 8 X. Wang and X. Zhong, “Transient growth of a Mach 5.92 flat-plate boundary layer,” **AIAA paper 2010-0535**, 2010.
- 9 X. Wang and X. Zhong, “Effect of porous coating on boundary-layer instability,” **AIAA**

- paper 2010-1243**, 2010.
- 10 A. Tumin, X. Wang, and X. Zhong, "Numerical simulation and theoretical analysis on hypersonic boundary-layer receptivity to wall blowing-suction," **AIAA paper 2010-0534**, 2010.
 - 11 J. Lei and X. Zhong, "Linear Stability Analysis of Nose Bluntness Effects on Hypersonic Boundary Layer Transition", **AIAA paper 2010-0898**, 2010.
 - 12 X. Wang and X. Zhong, "Nonequilibrium and reactive high-speed flow simulations with a fifth-order WENO scheme," **AIAA paper 2009-4041**, 2009.
 - 13 X. Wang and X. Zhong, "Numerical simulation and theoretical analysis on boundary-layer instability affected by porous coating," **AIAA paper 2009-3679**, 2009.
 - 14 L. Duan, X. Wang and X. Zhong "A High-Order Cut-Cell Method for Numerical Simulation of Hypersonic Boundary-Layer Transition with Arbitrary Surface Roughness", **AIAA paper 2009-1337**, January 2009.
 - 15 X. Wang and X. Zhong, "Effect of porous coating and its location on hypersonic boundary layer waves," **AIAA paper 2009-0942**, 2009.
 - 16 X. Zhong, "Numerical Simulation of Hypersonic Boundary Layer Receptivity and Stability on Blunt Circular Cones," **AIAA paper 2009-0940**, January 2009.
 - 17 J. Lei and X. Zhong, "Linear Stability Study of Hypersonic Boundary Layer Transition on Blunt Circular Cones," **AIAA paper 2009-939**, January 2009.
 - 18 L. Duan, X. Wang and X. Zhong "A High-Order Cut-Cell Method for Numerical Simulation of Hypersonic Boundary-Layer Instability with Surface Roughness", **AIAA paper 2008-3732**, June 2008.
 - 19 X. Wang, A. Tumin, and X. Zhong, "DNS and theoretical study of perturbations in a hypersonic boundary layer over a flat plate," **Bulletin of the American Physical Society**, Vol. 53, No. 15, pp. 180, 2008.
 - 20 X. Wang and X. Zhong, "Role of the synchronization point on boundary layer stabilization using porous coating," **AIAA paper 2008-4382**, 2008.
 - 21 X. Wang and X. Zhong, "Receptivity of A Hypersonic Flat-Plate Boundary Layer to Steady Blowing-Suction," **AIAA paper 2008-3731**, June 2008.

- 22 X. Wang and X. Zhong, "Receptivity of a Hypersonic Flat-Plate Boundary Layer to Surface Roughness," **AIAA paper 2008-0503**, Jan. 2008.
- 23 X. Wang and X. Zhong, "Numerical simulation of hypersonic boundary-layer receptivity to two and three-dimensional wall perturbations," **AIAA paper 2007-0946**, 2007.
- 24 X. Zhong, "Numerical Simulation of Surface Roughness Effects on Receptivity of Hypersonic Flow over Blunt Cones," **AIAA paper 2007-0944**, January 2007.

9 ACKNOWLEDGEMENT / DISCLAIMER

This work was sponsored by the Air Force Office of Scientific Research, USAF, under AFOSR Grant # FA9550-07-1-0414. The program manager is Dr. John Schmisser. The views and conclusions contained herein are those of the author and should not be interpreted as necessarily representing the official policies or endorsements either expressed or implied, of the Air Force Office of Scientific Research or the U.S. Government.

10 REFERENCES

1. Zhong, X., *High-Order Finite-Difference Schemes for Numerical Simulation of Hypersonic Boundary-Layer Transition*. Journal of Computational Physics, 1998. **144**: p. 662-709.
2. Wang, X., and Zhong, X., *Numerical simulation and theoretical analysis on boundary-layer instability affected by porous coating*. AIAA Paper 2009-3679, 2009.
3. Duan, L., Wang, X., and Zhong, X., *A High-Order Cut-Cell Method for Numerical Simulation of Hypersonic-Boundary Transition with Arbitrary Surface Roughness*. AIAA Paper 2009-1337, 2009.
4. Duan, L., and Zhong, X., *A High-Order Cut-Cell Method for Numerical Simulation of Three-Dimensional Hypersonic Boundary-Layer Transition with Finite Surface Roughness*. AIAA Paper 2010-1450, 2010.
5. Wang, X., and Zhong, X., *Effect of wall perturbations on the receptivity of a hypersonic boundary layer*. Physics of fluids, 2009. **21** (044101).
6. Wang, X., Tumin, A., and Zhong, X., *DNS and theoretical study of perturbations in a hypersonic boundary layer over a flat plate*. Bulletin of the American Physical Society, 2008. **53**(15): p. 180.
7. Zhong, X., and Ma, Y., *Boundary-layer receptivity of Mach 7.99 Flow over a blunt cone to free-stream acoustic waves*. Journal of Fluid Mechanics, 2006. **556**: p. 55-103.
8. Zhong, X., *Effect of Nose Bluntness on Hypersonic Boundary Layer Receptivity over a Blunt Cone*. AIAA paper 2005-5022, 2005.
9. Zhong, X., *Numerical Simulation and Experimental Comparison of Hypersonic Boundary Layer Instability over a Blunt Cone*. AIAA paper 2004-2244, 2004.
10. Zhong, X., *Numerical Simulation of Hypersonic Boundary Layer Receptivity and Stability*

- on Blunt Circular Cones. 2009, AIAA Paper 2009-0940.
11. Zhong, X., *Numerical Simulation of Surface Roughness Effects on Receptivity of Hypersonic Flow Over Blunt Cones* 2007, AIAA Paper 2007-0944.
 12. LeVeque, R., and Li, Z., *The immersed interface method for elliptic equations with discontinuous coefficients and singular sources*. SIAM Journal of Numerical Analysis, 1994. **31**: p. 1001-1025.
 13. Maslov, A.A., Shiplyuk, A. N., Sidorenko, A., and Arnal, D., *Leading-edge Receptivity of a Hypersonic Boundary Layer on a Flat Plate*. Journal of Fluid Mechanics, 2001. **426**: p. 73-94.
 14. Fedorov, A., Malmuth, N., Rasheed, A., and Hornung, H., *Stabilization of hypersonic boundary layers by porous coatings*. AIAA Journal, 2001. **39**(4): p. 605-610.
 15. Rasheed, A., Hornung, H., Fedorov, A., and Malmuth, N., *Experiments on passive hypervelocity boundary-layer control using an ultrasonically absorptive surface*. AIAA Journal, 2002. **40**(3): p. 481-489.
 16. Fedorov, A., Shiplyuk, A., Maslov, A., Burov, E., and Malmuth, N., *Stabilization of a hypersonic boundary layer using an ultrasonically absorptive coating*. Journal of Fluid Mechanics, 2003. **479**: p. 99-124.
 17. Maslov, A., *Stabilization of Hypersonic Boundary Layer by Microstructural Porous Coating*. IUTAM Symposium on One Hundred Years of Boundary Layer Research, 2006: p. 345-354.
 18. Egorov, I.V., Fedorov, A. V., and Soudakov, V. G., *Receptivity of a hypersonic boundary layer over a flat plate with a porous coating*. Journal of Fluid Mechanics, 2008. **601**: p. 165-187.
 19. Stetson, K.F., Thompson, E. R., Donaldson, J. C., and Siler, L. G., *Laminar Boundary Layer Stability Experiments on a Cone at Mach 8, Part 2: Blunt Cone*. AIAA paper 84-0006, 1984.
 20. Schneider, S.P., *Summary of hypersonic boundary-layer transition experiments on blunt bodies with roughness, J. Spacecraft and Rockets*. Journal of Spacecraft and Rockets, 2008. **45**: p. 1090-1112.
 21. Board, D.S., *Final report of the second defense science board task force on the national aero-space plane (NASP)*. 1992. p. 94-00052.
 22. Anderson, J.D., *Hypersonic and high temperature gas dynamics*. 2000: AIAA.
 23. Berry, S., Horvath, T., *Discrete roughness transition for hypersonic flight vehicles*, in *45th AIAA Aerospace Sciences Meeting and Exhibit*. 2007: Reno, Nevada.
 24. Saric, W.S., Reed, H. L., and Kerschen, E. J., *Boundary-Layer Receptivity to Freestream Disturbances*. Annual Review of Fluid Mechanics, 2002. **34**: p. 291-319.
 25. Boudreau, A.H., *Artificial Induced Boundary-Layer Transition on Blunt-Slender Cones at Hypersonic Speeds*. Journal of Spacecraft and Rockets, 1979. **16**(4): p. 245-251.
 26. Mahesh, K., *A family of high order finite difference schemes with good spectral resolution*. Journal of Computational Physics, 1998. **145**: p. 332-358.
 27. Poinot, T.J., and Lele, S. K., *Boundary conditions for direct simulations of compressible viscous flow*. Journal of Computational Physics, 1992. **101**(1): p. 104-129.
 28. Pruet, C.D.a.C., C. L., *Spatial direct numerical simulation of high-speed boundary-layer flows Part II: Transition on a cone in Mach 8 flow* Theoretical and Computational Fluid Dynamics, 1995. **7**: p. 397-424.

29. Lele, S.K., *Compact finite difference schemes with spectral-like resolution*. Journal of Computational Physics, 1992. **103**: p. 16-42.
30. Adams, N.A.S., K., *A High-Resolution Hybrid Compact-ENO Scheme for Shock-Turbulence Interaction Problems*. Journal of Computational Physics, 1996. **127**: p. 27-51.
31. Gaitonde, D.V., Visbal, M. R., *Further development of a Navier–Stokes solution procedure based on higher-order formulas*. AIAA Paper 1999-0557, 1999.
32. Zhong, X., *Leading-Edge Receptivity to Free Stream Disturbance Waves for Hypersonic Flow over a Parabola*. Journal of Fluid Mechanics, 2001. **441**: p. 315-367.
33. Fedkiw, R.P., Aslam, T.D., and Xu, S., *The Ghost Fluid Method for deflagration and detonation discontinuities*. Journal of Computational Physics, 1999. **154**(2): p. 393-427.
34. Udaykumar, H.S., Mittal, R., and Shyy, W. , *Computation of solid-liquid phase fronts in the sharp interface limit on fixed grids*. Journal of Computational Physics, 1999. **153**: p. 534-574.
35. Udaykumar, H.S., Mittal, R., Rampunggoon, P., and Khanna, A., *A Sharp Interface Cartesian Grid Method for Simulating Flows with Complex Moving Boundaries*. Journal of Computational Physics, 2001. **174**: p. 345–380.
36. Peskin, C., *The immersed boundary method*. Acta Numerica, 2002: p. 479-527.
37. Lee, L., LeVeque, R., *An immersed interface method for incompressible Navier-Stokes equations*. SIAM J. Sci. Computing, 2003. **25**: p. 832-856.
38. Marxen, O., Iaccarino, G., *Numerical simulation of the effect of a roughness element on high-speed boundary-layer instability*, in *38th Fluid Dynamics Conference and Exhibit*. 2008: Seattle, Washington.
39. Johansen, H., and Colella, P. , *A Cartesian Grid Embedded Boundary Method for Poisson's Equation on Irregular Domains*. Journal of Computational Physics, 1998. **147**: p. 60-85.
40. McCorquodale, P., Colella, P., and Johansen, H., *A Cartesian Grid Embedded Boundary Method for the Heat Equation on Irregular Domains*. . Journal of Computational Physics, 2001. **173**: p. 620-635.
41. Gibou, F., and Fedkiw, R.P., *A Fourth Order Accurate Discretization for the Laplace and Heat Equations on Arbitrary Domain with Applications to the Stefan Problem*. Journal of Computational Physics, 2005. **202**: p. 577-601.
42. Causon, D.M., Ingram, D. M., Mingham, C. G. , *A Cartesian cut cell method for shallow water flows with moving boundaries*. Advances in Water Resources, 2001. **24**: p. 899-911.
43. Dumett, M.A., Keener, J. P., *An immersed interface method for solving anisotropic elliptic boundary value problems in three dimensions*. SIAM J. Sci. Computing, 2003. **25**: p. 348-367.
44. Li, Z., *Immersed interface methods for moving interface problem*. Numerical Algorithms, 1997. **14**: p. 269-293.
45. Li, Z., *A fast iterative algorithm for elliptic interface problems*. SIAM J. Numer. Anal., 1998. **35**: p. 230-254.
46. Wiegmann, A., and Bube, K. P. , *The explicit-jump immersed interface method: finite difference methods for PDEs with piecewise smooth solutions*. SIAM J. Numer. Anal., 1998. **37**: p. 827-862.
47. Wiegmann, A., and Bube, K. P. , *The explicit-jump immersed interface method: finite*

- difference methods for PDEs with piecewise smooth solutions*. SIAM J. Numer. Anal., 2000. **37**: p. 827-862.
48. Huang, H., and Li, Z., *Convergence Analysis of the Immersed Interface Method*. IMA Journal of Numerical Analysis, 1999. **19**: p. 583-608.
 49. Fogelson, A.L., and Keener, J. P., *Immersed interface methods for Neumann and related problems in two and three dimensions*. . SIAM J. Sci. Computing, 2000. **22**: p. 1630-1654.
 50. Ito, K., Li, Z. , *Solving a nonlinear problem in magneto-rheological fluids using the immersed interface method*. Journal of Computational Physics, 2003. **19**: p. 253-266.
 51. Deng, S., Ito, K., Li, Z., *Three-dimensional elliptic solvers for interface problems and applications*. Journal of Computational Physics, 2003. **184**: p. 215–243.
 52. Adams, L., and Chartier, T. P. , *New geometric immersed interface multigrid solvers*. SIAM J. Sci. Computing, 2004. **25**: p. 1516-1533.
 53. Zhong, X., *A new high-order immersed interface method for multi-phase flow*. AIAA paper 2006-1294, 2006.
 54. LeVeque, R.J., and Li, Z., *Immersed interface methods for Stokes flow with elastic boundaries or surface tension*. SIAM J. Sci. Computing, 1997. **18**: p. 709-735.
 55. Berger, M.J., Leveque, R. J., *Stable boundary condition for Cartesian Grid calculations*. Computer System in Engineering, 1990. **1**: p. 305-311.
 56. Quirk, J.J., *An alternative to unstructured grids for computing gas dynamic flows around arbitrarily complex bodies*. Computers and Fluids, 1994. **23**: p. 125-142.
 57. Ghosh, S., Hossain, M. Matthaeus, W. H., *The application of spectral methods in simulating compressible fluid and magnetofluid turbulence*. Computer Physics Communications, 1993. **74**: p. 18-40.
 58. Zang, A., *Spectral methods next term for simulations of previous term transition next term and turbulence* Computer Methods in Applied Mechanics and Engineering, 1990. **80**(1-3): p. 209-221.
 59. Weller, H.G., Marooney, C.J., Gosman, A.D. , *A new spectral method for calculation of the time-varying area of a laminar flame in homogeneous turbulence*. Symposium on COMbustion, 1991. **23**: p. 629-636.
 60. Rai, M.a.M., P., *Direct numerical simulation of transition and turbulence in a spatially evolving boundary layer*. Journal of Computational Physics, 1993. **109**: p. 169-192.
 61. Fasel, H., Thumm, A., and Bestek, H. *Direct numerical simulation of transition in supersonic boundary layers: oblique breakdown*. in *Fluids Engineering Conference, Transitional and Turbulent Compressible Flows*. 1993. Washington, DC, June 20–24, 1993: ASME, New York.
 62. ADAMS, N.A., KLEISER, L., *Subharmonic transition to turbulence in a flat-plate boundary layer at Mach number 4.5*. Journal of Fluid Mechanics, 1996. **317**: p. 301-335.
 63. Pruet, C.D., *Spatial Direct Numerical Simulation of Transitioning High-Speed Flows*, in *Transitional and Turbulent Compressible Flows*, L.D. Kral, Spina, E. F., and Arakawa, C., Editor. 1995, ASME, FED-Vol. 224. p. 63-70.
 64. Zhu, L., Peskin, C. S., *Simulation of a flapping flexible filament in a flowing soap film by the immersed boundary method*. Journal of Computational Physics, 2002. **179**: p. 452-468.
 65. Malik, M.R., Lin, R. S., and Sengupta, R., *Computation of Hypersonic Boundary-Layer*

- Response to External Disturbances*. AIAA paper 1999-0411, 1999.
66. Ma, Y., and Zhong, X., *Receptivity to Freestream Disturbances of Mach 8 Flow over A Sharp Wedge*. AIAA paper 2003-0788, 2003.
 67. Whitehead, A.H., *Flow field and drag characteristics of several boundary-layer tripping elements in hypersonic flow*. Technical paper, NASA, 1969. **5454**.
 68. Lee, C.H., Chu, Y. H., *A New Type of TVD Schemes for Computations of High Speed Flows*, in *AIAA*. 1993.
 69. Ma, Y., and Zhong, X., *Receptivity of a Supersonic Boundary Layer over a Flat Plate. Part I: Wave Structures and Interactions*. Journal of Fluid Mechanics, 2003. **488**: p. 31-78.
 70. Wang, X.a.Z., X., *Numerical Simulation and Experiment Comparison of Leading-Edge Receptivity of a Mach 5.92 Boundary Layer*. AIAA paper 2006-1107, 2006.
 71. Tumin, A., Wang, X., and Zhong, X., *Direct numerical simulation and the theory of receptivity in a hypersonic boundary layer*. Physics of Fluids, 2007. **19**: p. 1-14.
 72. Mack, L.M., *Boundary layer linear stability theory*, in *AGARD Report*. 1984. p. 1-81.
 73. Maslov, A.A., Mironov, S. G., Shipliyuk, A. A., Sidorenko, A. A., Buntin, D. A., and Aniskin, V. M., *Hypersonic Flow Stability Experiments*. 2002. **AIAA 2002-0153**.
 74. Demetriades, A., *Hypersonic Viscous Flow Over A Slander Cone. Part III: Laminar Instability and Transition*. AIAA paper 74-535, 1974.
 75. Demetriades, A., *Laminar Boundary Layer Stability Measurements at Mach 7 Including Wall Temperature Effects*. AFOSR-TR-77-1311, 1977.
 76. Balakumar, P. *Transition In a Supersonic Boundary-Layer Due To Roughness Aand Acoustic Disturbances*. in *AIAA*. 2003.
 77. Malik, M.R., *Numerical methods for hypersonic boundary layer stability*. Journal of Computational Physics, 1990. **86**: p. 376-413.